Liquid Crystals
Publication details, including instructions for authors and subscription information:
http://www.informaworld.com/smpp/title~content=t713926090

Theory and numerical simulation of field-induced director dynamics in confined nematics investigated by nuclear magnetic resonance

A. F. Martins[a]; A. Véron[a]
[a] CENIMAT/I3N, Departamento de Ciência dos Materiais, Faculdade de Ciências e Tecnologia, Universidade Nova de Lisboa, Caparica, Portugal

Online publication date: 06 July 2010

To cite this Article Martins, A. F. and Véron, A.(2010) 'Theory and numerical simulation of field-induced director dynamics in confined nematics investigated by nuclear magnetic resonance', Liquid Crystals, 37: 6, 747 — 771
To link to this Article: DOI: 10.1080/02678292.2010.485837
URL: http://dx.doi.org/10.1080/02678292.2010.485837

Liquid Crystals,
Vol. 37, Nos. 6–7, June–July 2010, 747–771

Taylor & Francis
Taylor & Francis Group

INVITED ARTICLE

Theory and numerical simulation of field-induced director dynamics in confined nematics investigated by nuclear magnetic resonance

A.F. Martins* and A. Véron

CENIMAT/I3N, Departamento de Ciência dos Materiais, Faculdade de Ciências e Tecnologia, Universidade Nova de Lisboa, 2829-516 Caparica, Portugal

(*Received 13 January 2010; accepted 8 April 2010*)

We investigate the director reorientation in a nematic liquid crystal confined between two parallel plates and subjected to both a magnetic and an electric field. The permanent magnetic field is used first to align the director and, subsequently, to allow nuclear magnetic resonance (NMR) observation of the director response following the application of the electric field. For sufficiently strong electric fields, the director reorients and aligns parallel to the electric field. In this work we focus on the geometry where the electric and magnetic fields are orthogonal to each other. In this configuration the state of the system, immediately after applying the orthogonal electric field, is steady and unstable, at least in theory, since the director is assumed to be everywhere parallel to the magnetic field. In practice the real state of the system always deviates slightly from the perfect unstable steady state, which induces the start of the director reorientation toward the electric field. The nature and the characteristics of the initial deviation partially determine the reorientation process. In the classical approach, the small deviations from the ideal state are assumed to be due to thermal fluctuations, but this approach fails to account for some recent experimental results. For this reason we were led to investigate slightly non-uniform initial director configurations that are stable under the sole effect of the magnetic field but are sufficient to break the ideal unstable steady state created with the application of the orthogonal electric field. Such non-uniformities must be local or distributed over very small sample volumes, since their effects on the equilibrium NMR spectrum (before the application of the electric field) are not usually observed. In other words, we consider the presence of inversion walls in the bulk of the sample and local misalignments of the director on the boundary plates and investigate the effects of such non-uniformities on the response of the nematic to the application of the electric field, as observed by NMR. The model we propose, including such effects in parallel with thermal fluctuations, is able to account for the recently observed features of the field-induced director dynamics.

Keywords: nematic liquid crystal; Leslie–Ericksen; director reorientation; progressive mode; soliton mode

1. Introduction

It is of practical and theoretical interest to understand the response of a nematic liquid crystal initially close to an unstable steady state. Such configurations are easily obtained experimentally by applying an electric or a magnetic field on a previous stable state. A perfect unstable steady state is obtained when the field is applied normal to a fully aligned director field. However, in practice small deviations with respect to the perfect unstable steady alignment always arise, which causes the director reorientation toward a new steady state. The characteristics of the small initial deviations from perfect alignment dictate, at least partially, the subsequent time evolution. Until recently these initial deviations were always assumed to result from thermal fluctuations, i.e. small amplitude deviations extending over the whole sample. In a previous work we pointed out that the occurrence of a different kind of initial misalignments in real systems deserves to be considered; namely some strong and stable deviations localised in small regions of the sample [1, 2]. In this paper we detail some basic aspects of the previous results and explore the effects of a combination of both kinds of initial director deviations from perfect alignment.

When the misalignment of the director with respect to the direction imposed by the aligning magnetic field is only due to thermal fluctuations with small amplitudes, the reorientation following the sudden application of a sufficiently strong and orthogonal electric field (or a $\pi/2$ rotation of the sole magnetic field) manifests itself by the growing of one particular Fourier mode already present in the thermal fluctuation. Such a reorientation process has a typical deuterium nuclear magnetic resonance (NMR) signature: the initial quadrupolar doublet characterising the initially aligned sample gives rise to an additional broad doublet with *time-dependent splitting* while simultaneously the initial steady doublet with constant splitting progressively vanishes [3–5]. Some recent experimental data show NMR spectra with a different time evolution [6–8]. In this case, the application of the

*Corresponding author. Email: asfm@fct.unl.pt

ISSN 0267-8292 print/ISSN 1366-5855 online

DOI: 10.1080/02678292.2010.485837
http://www.informaworld.com

strong orthogonal electric field gives rise to the appearance of a new doublet with vanishing amplitude that progressively grows with *constant splitting* so that the total spectral intensity is essentially transferred from the initial doublet to the new one (with half the quadrupolar splitting). It should, however, be noted that non-negligible intensity arises in the central part of the later spectrum indicating some more complex behaviour. There are also experiments where the recorded spectra show some superposition of both features described here. These new results strongly suggest that the initial state is not simply homogeneous and perturbed by thermal fluctuations but some local inhomogeneities of the director field must be present in the initial state. Such non-uniformities must be local or distributed over very small sample volumes since their effects on the equilibrium NMR spectrum (before the application of the electric field) are not usually observed. It is, therefore, necessary to analyse the nematic response from an initial state exhibiting locally some strong misalignments of the director that moreover are stable under the effect of the initial aligning field. To this end, we will consider in this work two kinds of initial configuration: (i) in the first one (called C1 in later sections) the director is strongly anchored on one plate but the orientation of the easy axis on the plate exhibits some inhomogeneity around one point, or it is homogeneous but not parallel to the initial aligning field; (ii) in the second kind of configuration (called C2 in later sections) the director field exhibits several equidistant inversion walls normal to the plates.

More precisely, we consider a nematic liquid crystal, 4-n-pentyl-4′-cyanobiphenyl (5CB), confined between two parallel plates (electrodes). Initially a magnetic field parallel to the plates aligns the director everywhere except within regions with negligible volume (as compared with the sample volume). At time $t = 0$ an electric field normal to the plates is applied (via a voltage applied to the electrodes), whose magnitude is such that the alignment of the director with this field constitutes the new (fundamental) steady state. Briefly, in regions well-aligned with the magnetic field, the torque on the director is still vanishing while within the misaligned regions the director, already tilted toward the electric field, is subjected to a strong torque forcing the reorientation towards this field. Subsequently, a region already aligned forces adjacent regions to align as well, under the effect of curvature elasticity. However, this simple picture is usually perturbed by the occurrence of backflows in a complex way [3–5]. The purpose of this paper is to investigate accurately how the new steady state emerges from the initial one (with stable locally misaligned regions), eventually perturbed by thermal fluctuations. To simplify the analysis we will assume that the system is invariant by translation along the normal to the plane defined by the two orthogonal fields, which is certainly rather close to reality.

2. Theory

We now briefly give the main equations used in this work; they are directly derived from the equations of the Leslie–Ericksen theory [9, 10] when the inertial and convective terms are neglected. The material parameters of this theory are the Leslie viscosities α_i ($i = 1, \ldots, 6$) and the Frank elastic constants K_1, K_2 and K_3 [11]. It should be noted that the six Leslie viscosities are not independent since they satisfy the Parodi relation $\alpha_2 + \alpha_3 = \alpha_6 - \alpha_5$ [12]. It is, moreover, usual to define the additional viscous rotational coefficient $\gamma_1 = \alpha_3 - \alpha_2$.

The time evolution of the director $\mathbf{n}$ subjected to a flow with velocity $\mathbf{V}$ reads

$$\gamma_1 \frac{\partial n_i}{\partial t} = -\alpha_2 n_k V_{i,k} - \alpha_3 n_k V_{k,i} + h_i + \lambda n_i \quad i = 1, 2, 3, \tag{1}$$

where $\mathbf{h}$ is the molecular field [10] and λ is a Lagrange multiplier to account for the condition $\mathbf{n} \cdot \mathbf{n} = 1$ or equivalently $n_i \partial n_i / \partial t = 0$. The molecular field may be decomposed into an elastic and a field contribution, noted $\mathbf{h}^{el}$ and $\mathbf{h}^{field}$, respectively. The elastic contribution is given by

$$\begin{aligned} h_i^{el} = {} & K_2 n_{i,jj} + (K_1 - K_2) n_{j,ji} + (K_3 - K_2) n_j n_{i,j} n_{k,k} \\ & + (K_3 - K_2) n_j n_k n_{i,jk} + (K_3 - K_2) n_{i,j} n_k n_{j,k} \\ & - (K_3 - K_2) n_j n_{k,j} n_{k,i}. \end{aligned} \tag{2}$$

$i, j, k = 1, \ldots 3.$

When the sample is subjected to the magnetic and electric fields defined by

$$\begin{cases} \mathbf{B} = B\mathbf{u}_B & \forall t \\ \mathbf{E}(t) = E(t)\mathbf{u}_E \text{ with } \begin{cases} E(t) = 0 & \forall t < 0 \\ E(t) = E & \forall t > 0, \end{cases} \end{cases} \tag{3}$$

where $\mathbf{u}_B$ and $\mathbf{u}_E$ are two constant unit vectors, the field contribution $\mathbf{h}^{field}$ reads

$$\mathbf{h}^{field} = \frac{\chi_a}{\mu_0} B^2 [(\mathbf{n} \cdot \mathbf{u}_B)\mathbf{u}_B + \rho(\mathbf{n} \cdot \mathbf{u}_E)\mathbf{u}_E], \tag{4}$$

where

$$\rho(t) = \frac{\varepsilon_0 \mu_0 \varepsilon_a}{\chi_a} \left(\frac{E(t)}{B} \right)^2. \tag{5}$$

In Equations (4) and (5) μ_0 and ε_0 are the magnetic permeability and the dielectric permittivity of the vacuum, χ_a is the material's diamagnetic anisotropy and ε_a is the material's dielectric anisotropy. According to Equations (3) to (5) the magnitude of the electric field for $t > 0$ will be defined by the value of the dimensionless parameter ρ, namely, $\rho = 0$ for $t < 0$ and $\rho \neq 0$ for $t > 0$.

Within the assumptions used in this work, for any director configuration the velocity field cancels the divergence of the total stress tensor σ_{ij} (i.e. the force density vanishes everywhere), which reads $\sigma_{pi,p} = 0$ (i, $p = 1, 2, 3$). The total stress tensor is the sum of a viscous contribution, σ^{v}_{ij}, and an elastic contribution, σ^{el}_{ij}, defined by

$$\sigma^{v}_{ij} = \eta_{ijpq} V_{p,q} + \alpha_2 n_i \omega_j + \alpha_3 n_j \omega_i \quad i,j,p,q = 1,2,3 \quad (6)$$

and

$$\begin{aligned}\sigma^{e}_{ij} = &-K_2 n_{k,i} n_{k,j} - (K_1 - K_2) n_{l,l} n_{i,j} \\ &- (K_3 - K_2) n_i n_l n_{k,l} n_{k,j} \quad i,j,p,q = 1,2,3.\end{aligned} \quad (7)$$

In Equation (6) ω_i stands for the director velocity $\partial n_i/\partial t$ and η_{ijpq} ($i, j, p, q = 1, 2, 3$) denotes some general viscous coefficients that, within the scope of the Leslie–Ericksen theory, take the following particular form:

$$\eta_{ijpq} = \frac{1}{2}\left\{\begin{array}{l} 2\alpha_1 n_i n_j n_p n_q + \alpha_4\left(\delta_{ip}\delta_{jq} + \delta_{iq}\delta_{jp}\right) \\ +(\alpha_5 + \alpha_2) n_i n_p \delta_{jq} + (\alpha_5 - \alpha_2) n_i n_q \delta_{jp} \\ +(\alpha_6 + \alpha_3) n_j n_p \delta_{iq} + (\alpha_6 - \alpha_3) n_j n_q \delta_{ip} \end{array}\right\} \quad i,j,p,q = 1,2,3. \quad (8)$$

The equation $\sigma_{pi,p} = 0$ (i, $p = 1, 2, 3$) determining the velocity (for a given director configuration) may be cast in the form

$$\mu_{ijkl} V_{j,kl} + \nu_{ijk} V_{j,k} + S_i - P_{,i} = 0 \quad i,j,k,l = 1,2,3, \quad (9)$$

where

$$\left\{\begin{array}{l} \nu_{ijk} = \eta_{pijk,p} \\ \mu_{ijkl} = \eta_{kijl} \end{array}\right. \quad i,j,k,l,p = 1,2,3. \quad (10)$$

In Equation (9) P denotes the pressure and the vector $\mathbf{S}$ is defined by

$$S_i = \frac{\partial}{\partial x_p}\left(\alpha_2 n_p \omega_i + \alpha_3 n_i \omega_p\right) + \sigma^{e}_{pi,p} \quad i,p = 1,2,3. \quad (11)$$

Equation (9) possesses the following property: in the absence of external cause of flow, such as shearing or imposed pressure gradient, the velocity is non-null if and only if the vector field $\mathbf{S}$ is not purely irrotational (i.e. $\nabla \times \mathbf{S} \neq 0$). Indeed for an irrotational field $\mathbf{S}$ a scalar field F exists such that $\mathbf{S} = \nabla F$, in this case $\mathbf{V} = \mathbf{0}$ with $P = F$ solves Equation (9) and satisfies the convenient boundary conditions. Conversely $\mathbf{V} = \mathbf{0}$ entrains $\mathbf{S} = \nabla P$ and $\mathbf{S}$ would be irrotational. It appears that the vector $\mathbf{S}$ is responsible for the back-flow. By analogy with a Poisson equation, the term $\mathbf{S}$ is called a source term; note that such a term is absent from classical hydrodynamics.

It is worth recalling that without external source of flow the velocity vanishes for any steady inhomogeneous director field, i.e. a director field satisfying $h_i + \lambda\, n_i = 0$. In this case $\partial\mathbf{n}/\partial t = \mathbf{0}$ and $\mathbf{S}$ reduces to the divergence of the Ericksen stress tensor. Since this latter quantity does not vanish for an inhomogeneous steady director one might expect occurrence of flow; it is actually not the case because the divergence of the Ericksen stress tensor is an irrotational field for any steady director configuration (see note 1) [10].

3. Results and discussion

3.1 Description of the investigated system

We consider a nematic liquid crystal confined between two parallel plates a distance d apart as shown in Figure 1. Before starting the director reorientation, the sample is subject to a magnetic field that aligns the director in the most part of it. At time $t = 0$ an electric field normal to the plates is applied with a magnitude strong enough to dominate the magnetic field and to force the director to align parallel to the electric field. According to this geometry (see Figure 1) the system may be seen as bidimensional, since the director is maintained within the plane defined by the two fields; for that reason this plane is chosen as the 2D domain of integration and consequently the gradients arising normal to this plane are neglected. The x_1 axis and the associated unit vector $\mathbf{e}_1$ are chosen normal to the plates while the x_2 axis and the unit vector $\mathbf{e}_2$ are chosen parallel to the plates in such a way that the magnetic field lies within the plane (x_1, x_2). The x_3 axis and the unit vector $\mathbf{e}_3$ are chosen in order to get a right-handed system of axes. It follows that Equation (1) must be solved with the additional conditions n_3, $n_{i,3} = 0$ and $n_{i,j3} = 0$ (i, $j = 1, 2, 3$).

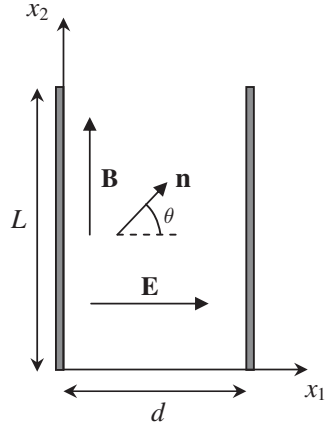

Figure 1. Geometry used in this work. The electric field, **E**, is normal to the plates and parallel to the x_1 axis, while the magnetic field, **B**, is parallel to the plates.

Moreover, the absence of gradients along x_3 also applies to the velocity for consistency. It turns out that the assumptions for the director entrain a particular structure for the coefficients μ_{ijkl} and ν_{ijk} in Equation (9) such that the component V_3 appears uncoupled to the two other components; remarking moreover that we also have $S_3 = 0$ for the homogeneous director along the x_3 axis, it follows that $V_3 = 0$ with $P_3 = 0$ solves Equation (9) for $i = 3$. Accordingly, the three dimensional system of equations formed by Equations (1) and (9) reduces to a two-dimensional system of equations within the plane (x_1, x_2). The domain of numerical integration is defined by $0 < x_1 < d$, with d the distance between the plates and $0 < x_2 < L$, where L is not necessarily the length of the real cell.

The magnetic and electric fields being parallel and normal to the plates, respectively, the general Equation (4) may be particularised by setting $\mathbf{u}_B = \mathbf{e}_2$ and $\mathbf{u}_E = \mathbf{e}_1$, which yields

$$\mathbf{h}^{field} = \frac{\chi_a}{\mu_0} B^2[(\rho - 1)n_1\mathbf{e}_1 - n_3\mathbf{e}_3 + \mathbf{n}]. \qquad (12)$$

Remarking that the term proportional to $\mathbf{n}$ in Equation (12) may be dropped (see note 2) and considering a director lying within the plane (x_1, x_2), the field contribution to the molecular field reduces to

$$\mathbf{h}^{field} = \frac{\chi_a}{\mu_0} B^2(\rho - 1)n_1\mathbf{e}_1. \qquad (13)$$

It appears that for $\rho > 1$ the superposition of the two external fields is equivalent to one single effective aligning field normal to the plates and with the magnitude $\sqrt{\rho - 1}\,B$. It follows that when an electric field corresponding to $\rho > 1$ is applied, the previous state becomes unstable. On the other hand, it is worth noting that switching the electric field on corresponding to $\rho = 2$ is (almost) equivalent to rotating the magnetic field by $\pi/2$.

Equations (1) and (9) are solved with the following boundary conditions. For the free boundaries at $x_2 = 0$ or $x_2 = L$ periodic boundary conditions are used for the velocity and the director. Given that the source term $\mathbf{S}$ in Equation (9) involves the spatial derivative of $\boldsymbol{\omega} = \partial\mathbf{n}/\partial t$ we also need boundary conditions for $\boldsymbol{\omega}$ at $x_2 = 0$ or $x_2 = L$, they must be periodic as well in order to be consistent with the boundary conditions for the director. On the bounding plates (i.e. at $x_1 = 0$ and $x_1 = d$) the velocity vanishes and the director is rigidly anchored for the configuration C1 or weakly and homeotropically anchored for the configuration C2. More precisely, for the configuration C1 we take $\mathbf{n} = (0,1,0)$ on the plate at $x_1 = d$ while the x_2 dependence of the director on the plate at $x_1 = 0$ is defined by

$$\begin{cases} n_1 = \cos\theta \\ n_2 = \sin\theta \\ n_3 = 0 \end{cases}, \qquad (14)$$

with

$$\theta(x_2) = \frac{\pi}{2} - \left\{\theta_0 + A\exp\left(-\frac{1}{2}\left(\frac{x_2 - x_{20}}{\sigma}\right)^2\right)\right\}. \qquad (15)$$

This Equation (15) defines a misalignment of the director over the plate, centred at $x_2 = x_{20}$ with amplitude A and spatial extension σ. The parameter θ_0 determines the director orientation over the plate outside the misalignment region (i.e. for $|x_2 - x_{20}| >> \sigma$); for $\theta_0 = 0$ the anchoring is parallel to the plate, while for $\theta_0 = \pi/2$ it is homeotropic. We might consider that the localised misalignment centred at $x_1 = 0$, $x_2 = x_{20}$ is actually the trace in the plane (x_1, x_2) of a misalignment extended around a straight line parallel to the x_3 axis (for simplicity). If the misalignment is quite homogeneous along this line, i.e. along the x_3 axis, we might expect some homogeneity of the flow along the part of the x_3 axis where the misalignment exists. This kind of extended misalignment is in good agreement with the assumption of null gradient along x_3 used in this work. Finally, a physical meaning might be attributed to the parameter L; it might be the mean length separating neighbouring misaligned regions on the plate. With this interpretation of L it is sufficient to perform a simulation for a domain with length L and containing just *one* misalignment region.

Concerning the configuration C2, the inversion walls are generated by using the function

$$\Theta(y) = \tan^{-1}\left(\sinh\left(\frac{y}{L_c}\right)\right) \qquad (16)$$

with

$$L_c = \left(\frac{\chi_a}{\mu_0}\frac{B^2}{K}\right)^{-1/2}, \qquad (17)$$

which is a solution of the differential equation $L_c^2 d^2\theta/dy^2 + \sin\theta\cos\theta = 0$; this latter equation is a particular case of Equation (1) with $\mathbf{V} = \mathbf{0}$, $\mathbf{n}$ given by Equation (14) and the spherical approximation, i.e. $K_1 = K_2 = K_3 = K$. Remarking that Θ varies from $-\pi/2$ for $y \to -\infty$ to $+\pi/2$ for $y \to +\infty$ it appears that, in the first approximation, $\Theta(y)$ defined by Equation (16) describes one inversion wall placed at the origin and L_c is a characteristic length determining the depth of the wall. A configuration with several walls may be defined by superposing the functions $\Theta(y-y_k)$ where y_k denotes the position of the k^{th} wall via

$$\theta(y) = \sum_k (-1)^k \Theta(y - y_k). \tag{18}$$

The alternate signs in Equation (18) yield a set of walls in which the director alternatively rotates by $+\pi$ or $-\pi$ when the coordinate y increases. For both systems an analytical director profile is used to start the numerical calculations, but actually this profile is not exactly stationary; for that reason in a preliminary stage Equation (1) is solved with $\mathbf{V} = \mathbf{0}$, $\rho = 0$ and with the analytical profile used as the initial condition in order to relax it toward the steady profile closest to the analytical one. At the end of this stage we obtain the steady initial state exhibiting some local misalignment.

A thermal fluctuation of θ around θ_0 is defined by considering the Fourier series decomposition of $\theta - \theta_0$; we find

$$\theta(x_1, x_2) = \theta_0 + \sum_{n=0}^{N}\sum_{m=0}^{M} A_{nm} \sin\left(nq_1 x_1 + \phi_n^{(1)}\right) \sin\left(mq_2 x_2 + \phi_m^{(2)}\right), \tag{19}$$

with $A_{00} = 0$, $q_1 = 2\pi/d$, $q_2 = 2\pi/L$ and where N and M denote the number of modes necessary in practice to describe the fluctuation. For $|\theta - \theta_0| << \pi$ the total free energy F reads (see note 3):

$$\mathsf{F} = \sum_{n=0}^{N}\sum_{m=0}^{M} F_{nm}(\theta_0) A_{nm}^2 \tag{20}$$

with

$$\mathsf{F}_{nm}(\theta_0) = \frac{dL^2}{4}\left[\begin{array}{l}(1+\delta_{m0})F_1(\theta_0)n^2q_1^2 + (1+\delta_{n0})F_2(\theta_0)m^2q_2^2 \\ +\frac{\chi_a}{\mu_0}(\rho-1)B^2(1+\delta_{n0}+\delta_{m0})G(\theta_0)\end{array}\right] \tag{21}$$

and

$$\begin{cases} F_1(\theta) = \frac{1}{2}\left(K_1 \sin^2\theta + K_3 \cos^2\theta\right) \\ F_2(\theta) = \frac{1}{2}\left(K_1 \cos^2\theta + K_3 \sin^2\theta\right) \\ G(\theta) = \frac{1}{2}\left(\cos^2\theta - \sin^2\theta\right). \end{cases} \tag{22}$$

It follows from Equation (20) that the probability distribution of each amplitude A_{nm} according to statistical mechanics is Gaussian with null mean value and its variance σ_{nm}^2 is given by

$$\sigma_{nm}^2 = \frac{k_B T}{2\mathsf{F}_{nm}}, \tag{23}$$

where k_B denotes the Boltzmann constant and T the temperature. It is worth noting that the expression for σ_{nm}^2, i.e. the mean value of A_{nm}^2, entrains the mean energy $k_B T/2$ per mode (see Equations (20) and (23)), in agreement with the equipartition of energy theorem. Concretely, one thermal fluctuation is generated numerically by generating random numbers A_{nm} with the adequate Gaussian distribution. On the other hand, since the phases $\phi_n^{(1)}$ and $\phi_m^{(2)}$ do not appear in the total free energy (see Equations (20) to (22)), they are uniformly distributed over the interval $[0, 2\pi]$. With these equations we can find that the mean amplitude of $|\theta - \theta_0|$ is very small ($\sim 0.1^\circ$), presumably because the modes with wave vector parallel to the x_3 axis are neglected in the two-dimensional approach used here. Accordingly, the expression of $\theta - \theta_0$ given by Equation (19) is multiplied by an ad-hoc coefficient that, moreover, allows us to adjust the amplitude of the fluctuations. In this work this ad-hoc coefficient has been fixed in such a way to obtain fluctuations with magnitudes of the order of 1°.

For $t \geq 0$, Equation (1) for the director and Equation (9) for the velocity are solved iteratively, i.e. the director (velocity) equation is solved at each step with the velocity (director) field obtained at the previous step. The director equation is solved by using the fourth order Runge–Kutta explicit scheme, and the velocity equation is solved by using the Successive Over-Relaxation iterative scheme, while evaluating the pressure by solving a Poisson equation [13]. The results discussed in this work have been obtained with (i) the material coefficients of 5CB at $T_{NI} - T = 10^\circ$C [13, 14] given here in Table 1, (ii) the field parameters $B = 4$ T, $\rho = 2$ and $\chi_a/\mu_0 = 1.14$ and (iii) the geometrical parameters $d = 50\,\mu$m, $L = 100\,\mu$m, $L = 200\,\mu$m or $L = 250\,\mu$m, $x_{20} = L/2$ and $\sigma = 5\,\mu$m. The value of d corresponds to a real set-up while the choice of L is a compromise between time consuming considerations and the assumption that L should be much larger than d. For the configuration C1 several sets of parameters have been used, namely, $\theta_0 = 0$ with $A = 0.8$, $\theta_0 = \pi/4$ with $A = 0$ and $\theta_0 = \pi/4$ with $A = 0.8$. For the configuration C2, two and four inversion walls have been considered. Concerning the numerical parameters, we have used the time increment $\Delta t = 15\,\mu$s and the space increments $\Delta x_1 = \Delta x_2 = 0.31\,\mu$m.

Table 1. Material parameters for 5CB at $T_{NI} - T = 10^\circ$C.

Leslie viscosities [14]	Frank elastic constants [15]
$\alpha_1 = -0.006$Pa s^{-1}	$K_1 = 1.15 \times 10^{-11}$N
$\alpha_2 = -0.081$Pa s^{-1}	$K_2 = 0.60 \times 10^{-11}$N
$\alpha_3 = -0.005$Pa s^{-1}	$K_3 = 1.53 \times 10^{-11}$N
$\alpha_4 = 0.065$Pa s^{-1}	
$\alpha_5 = 0.064$Pa s^{-1}	
$\alpha_6 = -0.022$Pa s^{-1}	

3.2 The primary and secondary initial states

The electric field is applied at time $t = 0$ on an equilibrium state. Since we neglect inertia in both equations for the director and the velocity we are led to distinguish the state at time $t = 0^+$ immediately after applying the electric field from the equilibrium state at time $t = 0^-$ immediately before; it is because a flow develops 'instantaneously' under this approximation. Accordingly, we call primary and secondary initial states the states at times $t = 0^-$ and $t = 0^+$, respectively. In the primary initial state there is no flow and the director satisfies the equation $h_i + \lambda n_i = 0$ with $\rho = 0$ (see Equation (1)) and the boundary conditions for the director specified in Section 3.1. In the secondary initial state the director profile is identical to that of the primary state (there is no change in the director field during an infinitesimal interval of time), but the director velocity $\boldsymbol{\omega} = \partial \mathbf{n}/\partial t$ becomes suddenly non-null because of the sudden increase of the coefficient ρ in the molecular field at time $t = 0$. The inhomogeneous director profile implies an inhomogeneous director velocity $\boldsymbol{\omega}$ that, except for a very particular case, surely implies a non purely irrotational source term $\mathbf{S}$ in the velocity equation (Equation (9)); accordingly, we also expect $\mathbf{V} \neq \mathbf{0}$ as soon as $\rho \neq 0$ in the presence of an arbitrary misalignment in the director field. It is, however, not sufficient to stop the reasoning at this point; indeed the non-null velocity requires a revaluation of the director velocity, $\boldsymbol{\omega}$, because this latter quantity depends on the velocity gradients (see Equation (1)). In conclusion, to characterise fully the secondary initial state requires solving a set of two coupled equations for $\mathbf{V}$ and $\boldsymbol{\omega}$ while maintaining the director fixed.

The particular iterative procedure used to evaluate $\mathbf{V}$ and $\boldsymbol{\omega}$ at time $t = 0^+$ is described in more detail here. According to Equation (1) at time $t = 0^-$ the equilibrium is expressed by

$$\mathbf{h}_-^{el} + (\chi_a/\mu_0)B^2(\mathbf{n}_- \cdot \mathbf{u_B})\mathbf{u_B} + \lambda^{(0)}\mathbf{n}_- = \mathbf{0}$$

(the subscript – (+) indicates that the quantities are evaluated at time $t = 0^-$ ($t = 0^+$)). A first evaluation of $\boldsymbol{\omega}$ at time $t = 0^+$, noted $\boldsymbol{\omega}_+^{(1)}$, is obtained by setting $\rho \neq 0$ in Equation (4), which yields,

$$\gamma_1 \boldsymbol{\omega}_+^{(1)} = \mathbf{h}_-^{el} + (\chi_a/\mu_0)B^2(\mathbf{n}_- \cdot \mathbf{u}_B)\mathbf{u}_B + (\chi_a/\mu_0)B^2\rho(\mathbf{n}_- \cdot \mathbf{u_E})\mathbf{u_E} + \lambda^{(1)}\mathbf{n}$$

thus use of the previous equilibrium relation yields

$$\gamma_1 \boldsymbol{\omega}_+^{(1)} = (\chi_a/\mu_0)B^2\rho(\mathbf{n}_- \cdot \mathbf{u_E})\mathbf{u_E} + \left(\lambda^{(1)} - \lambda^{(0)}\right)\mathbf{n}_-$$

where $\lambda^{(1)} - \lambda^{(0)}$ is the Lagrange multiplier associated with the condition $\boldsymbol{\omega}_+^{(1)} \cdot \mathbf{n}_- = 0$. Inserting $\boldsymbol{\omega}_+^{(1)}$ in Equation (9) and solving this equation yields a first evaluation of the flow velocity, denoted by $\mathbf{V}_+^{(1)}$. It follows that $\boldsymbol{\omega}_+^{(1)}$ cannot represent the true director velocity since it has been evaluated with the wrong velocity $\mathbf{V} = \mathbf{0}$; a better evaluation of $\boldsymbol{\omega}_+$, denoted by $\boldsymbol{\omega}_+^{(2)}$, is given by

$$\gamma_1 \boldsymbol{\omega}_{+i}^{(2)} = -\alpha_2 \mathrm{n}_{-k} V_{+i,k}^{(1)} - \alpha_3 n_{-k} V_{+k,i}^{(1)} + (\chi_a/\mu_0)\mathrm{B}^2\rho(\mathbf{n}_- \cdot \mathbf{u}_\mathrm{E})\mathbf{u}_\mathrm{E} \cdot \mathbf{e}_\mathrm{i} + \lambda^{(2)}\mathbf{n}_- \cdot \mathbf{e}_\mathrm{i}.$$

Now a new evaluation of the flow velocity, denoted by $\mathbf{V}_+^{(2)}$, is obtained by solving Equation (9) with $\boldsymbol{\omega}_+^{(2)}$ replacing $\boldsymbol{\omega}_+^{(1)}$, and so forth. It is necessary to iterate this procedure several times because the jump in $\mathbf{V}$ and $\boldsymbol{\omega}$ between $t = 0^-$ and $t = 0^+$ is large since the jump in ρ is large; in practice we found that ten iterations were sufficient when ρ jumps from 0 to 2. In summary, the numerical procedure is divided into three stages. In a first stage the primary initial state is calculated by relaxing an *ad hoc* director field under the effect of the magnetic field and the anchoring. In the second stage the director and flow velocities of the secondary initial state are calculated. Finally, in the third stage the classical resolution of Equations (1) and (9) is performed by using the secondary initial state as the initial condition for the relaxation when the electric field is on ($\rho = 2$).

Given that $\mathbf{n}_-$, the director at time $t = 0^-$, is neither parallel nor perpendicular to $\mathbf{u}_\mathrm{E}$ within the misalignment region, it follows that $\boldsymbol{\omega}_+^{(1)}$ does not vanish on the plate at $x_1 = 0$ and around $x_2 = x_{20}$, in contradiction with rigid anchoring. However, it should be noted that the real director velocity is given by

$$\gamma_1 \boldsymbol{\omega}_{+i} = -\alpha_2 n_{-k} V_{+i,k} - \alpha_3 n_{-k} V_{+k,i} + (\chi_a/\mu_0)B^2\rho(\mathbf{n}_- \cdot \mathbf{u}_\mathrm{E})\mathbf{u}_\mathrm{E} \cdot \mathbf{e}_\mathrm{i} + \lambda \mathbf{n}_- \cdot \mathbf{e}_\mathrm{i}.$$

Since the velocity gradients do not vanish on the plate, we may expect to find $\boldsymbol{\omega} \to \mathbf{0}$ when we approach the plate within the misaligned region. Actually, we note that $\boldsymbol{\omega}_+$ is given by an analytical relation (not a differential equation) so that the boundary condition for $\boldsymbol{\omega}$ is never taken into account in evaluating $\boldsymbol{\omega}_+$ and consequently this condition has no reason to be satisfied at time $t = 0^+$. Despite this feature, the velocity is continuous on the plate, probably because the boundary condition for the velocity is taken into account when solving Equation (9). Remarking, moreover, that the discontinuity of $\boldsymbol{\omega}$ vanishes for $t > 0^+$ we did not consider this problem as serious.

3.3 The velocity profile at time $t = 0^+$ in the configuration C1

Figure 2(a) shows the 2D profile of the initial director misalignment consistent with the boundary condition defined by Equation (15). The director is represented

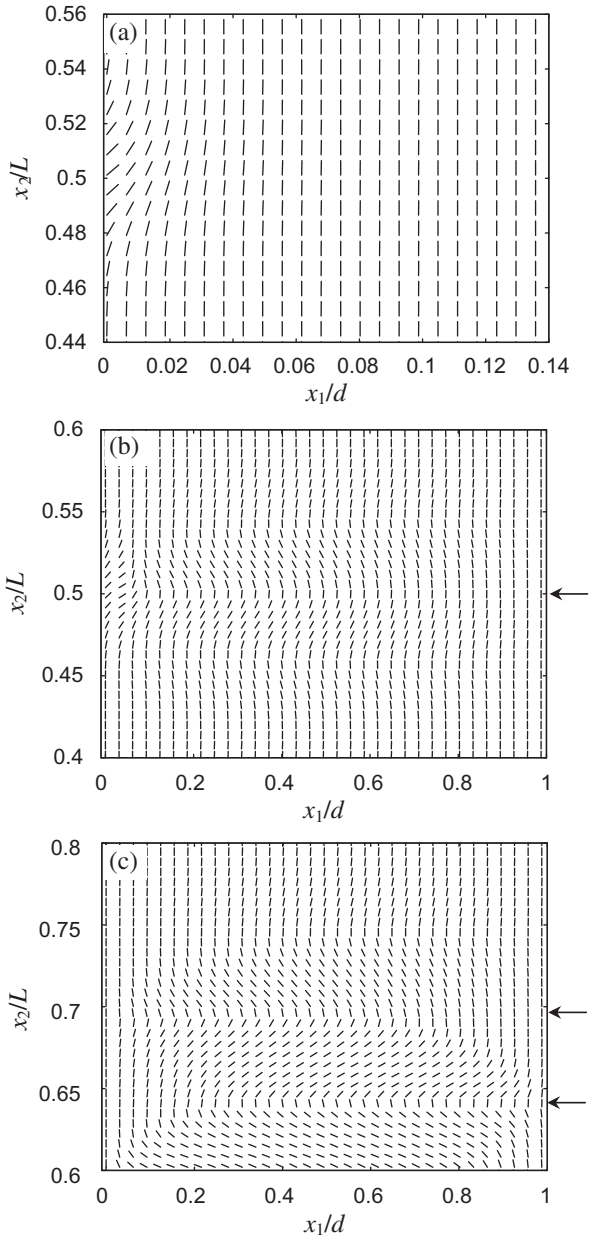

Figure 2. 2D profile of the director at time $t = 0^-$ (a), time $t = 7.5$ ms (b) and time $t = 15.75$ ms (c) in a region of the sample where the misalignment is strong. The misalignment on the plate is defined by Equations (12) and (13) with $\theta_0 = 0$, $x_{20} = L/2$ and $A = 0.8$. The steady director field has been obtained with $B = 4$ T. The arrows indicate the position of inversion walls.

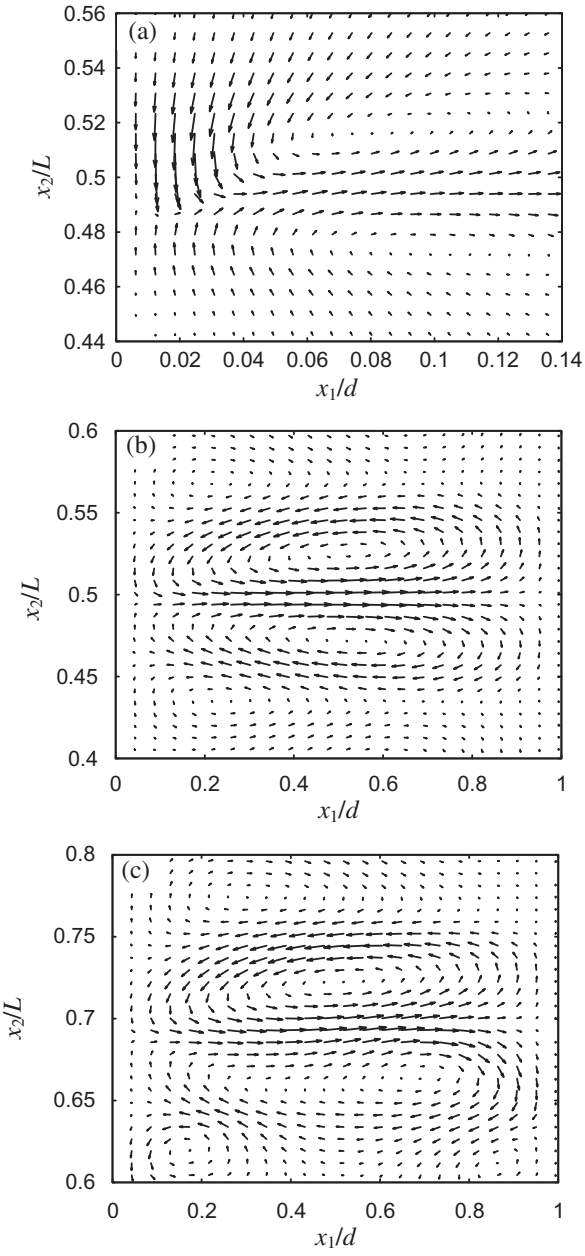

Figure 3. 2D profile of the velocity at time $t = 0^+$ (a), time $t = 7.5$ ms (b) and time $t = 15.75$ ms (c) in the vicinity of the director misalignment shown in Figure 2.

by a rod with constant length because **n** is physically equivalent to $-\mathbf{n}$ and $n_3 = 0$. Only the vicinity of the misalignment centred at $x_1 = 0$ and $x_2 = x_{20} = L/2$ is represented, namely within the domain defined by $0 \leq x_1/d \leq 0.14$ and $0.44 \leq x_2/L \leq 0.56$. Obviously, within the part of the domain not represented in Figure 2(a), the director is parallel to the magnetic field (i.e. the rods are vertical). The profile at $x_1 = 0$ is given by Equations (12) and (13) with $\theta_0 = 0$ and $A = 0.8$. The profile for $x_1 > 0$ has been obtained by relaxation of the director under the magnetic field and assuming rigid anchoring on the plate. Figure 3a shows the 2D profile of the velocity in the same domain as for the director profile in Figure 2(a). Unfortunately, due to a great variation of the magnitude of the velocity within the sample, it is difficult to visualise the stream lines over a large region with this graphic representation. For that reason we show in Figure 4 a normalised velocity field at time $t = 0^+$, i.e. the field $\mathbf{V}/||\mathbf{V}||$, it is

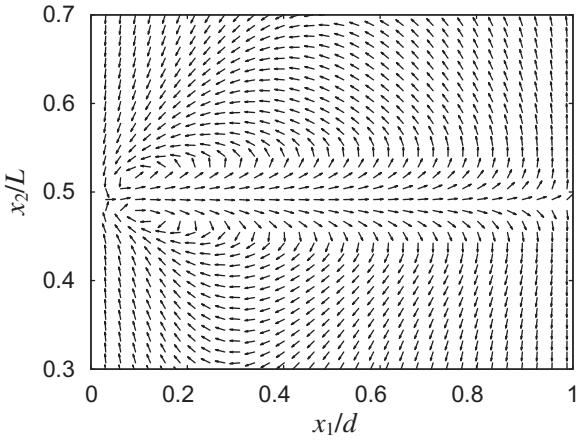

Figure 4. Stream lines at time $t = 0^+$ evidenced by plotting the 2D profile of $\mathbf{V}/||\mathbf{V}||$.

represented by arrows with constant length indicating the direction of flow. It appears that the velocity field at time $t = 0^+$ is characterised by the occurrence of two adjacent rolls with opposite vorticity in the vicinity of the misaligned region. The two initial rolls are not symmetric as shown in Figures 3(a) and 4; this is because the initial director profile is not symmetric as well (see Figure 2(a)). Although by construction of the anchoring orientation defined by Equation (13) the function $\theta(x_2)$ is even with respect to x_{20}, i.e. it exhibits a mirror plane at $x_2 = x_{20}$, no symmetry occurs for the director (e.g. we should have $n_1(x_2)$ even and $n_2(x_2)$ odd to obtain a mirror plane normal to the plates).

Some qualitative features concerning the velocity field at time $t = 0^+$ may be understood as follows. A null velocity field is not expected because the source term has no reason to be irrotational for an arbitrary misalignment (see end of Section 2). The occurrence of rolls in the velocity field is dictated by the incompressibility condition $V_{1,1} + V_{2,2} = 0$, the boundary conditions and the additional assumption that the velocity should vanish sufficiently far from the misaligned region, i.e. for $x_2 \to \pm\infty$. These conditions entrain that both functions $V_1(x_1, x_2)$ and $V_2(x_1, x_2)$ must be non-null, as expected for rolls. Indeed, because of the incompressibility condition the assumption $V_1 = 0$ everywhere entrains $V_{2,2} = 0$ or $V_2 = f(x_1)$, but since V_2 should vanish for $x_2 \to \pm\infty$, we obtain $V_2 = 0$ and finally $\mathbf{V} = \mathbf{0}$. Likewise, assuming $V_2 = 0$ everywhere entrains $V_{1,1} = 0$ or $V_1 = g(x_2)$, but since $V_1 = 0$ on the plates (i.e. $x_1 = 0$ and $x_1 = d$), we find $V_1 = 0$ and finally $\mathbf{V} = \mathbf{0}$. On the other hand, the total transversal flux (flux along x_1) and the total longitudinal flux (flux along x_2) vanish, which mathematically reads $\int V_1(x_1, x_2)dx_2 = 0 \ \forall x_1$ and $\int V_2(x_1, x_2)dx_1 = 0 \forall x_2$. These integral relations imply that V_1 as a function of x_2 and V_2 as a function of x_1 must take both negative and positive values, which is compatible with occurrence of rolls. Finally, the opposite vorticity between adjacent rolls allows minimising frictions.

An important feature evidenced at time $t = 0^+$ is the fact that the spatial extension of the initial flow is much larger than the spatial extension of the misaligned region, in particular the transversal extension. When we compare Figures 2(a) and 3(a) it appears that the alignment is perfect for $x_1/d > 0.03$ while a non-negligible flow still occurs for $x_1/d > 0.14$. Figures 5 and 6 show the transversal profile of n_1, V_1, V_2 and $||\mathbf{V}||$ at $x_2/L = 0.5$ (i.e. where the misalignment is stronger, as shown in Figure 2(a)) for different times. The spatial extension of any quantity may be defined as the length of space interval where the quantity is larger than 10% of its maximum value. Applying this definition to $||\mathbf{V}||$ we find that at time $t = 0^+$ the transversal extension of the flow is one order of magnitude larger than the transversal extension of the misalignment. In contrast, the longitudinal extensions of the flow and of the misalignment have the same order of magnitude. We note that the maximum of V_1 for $x_2/L = 0.5$ lies at $x_1/d = 0.077$ where the value of n_1 is about 1% of its maximum value at $x_1 = 0$; on the other hand, the maximum of $|V_2|$ for $x_2/L = 0.5$ lies at $x_1/d = 0.016$, where the value of n_1 is about 40% of its maximum value. Accordingly, a non-negligible part of the initial flow lies outside the misaligned region.

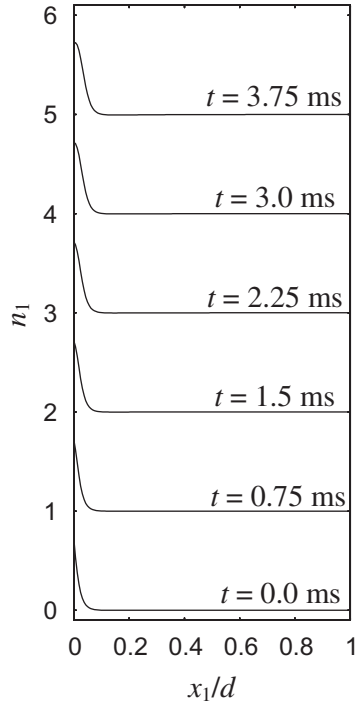

Figure 5. Profiles along the x_1 axis of n_1 at $x_2/L = 0.5$ (a) for different times; for clarity, the curves are translated by a multiple of 1. Calculated with $B = 4$ T, $\rho = 2$, $L = 250$ μm and $d = 50$ μm.

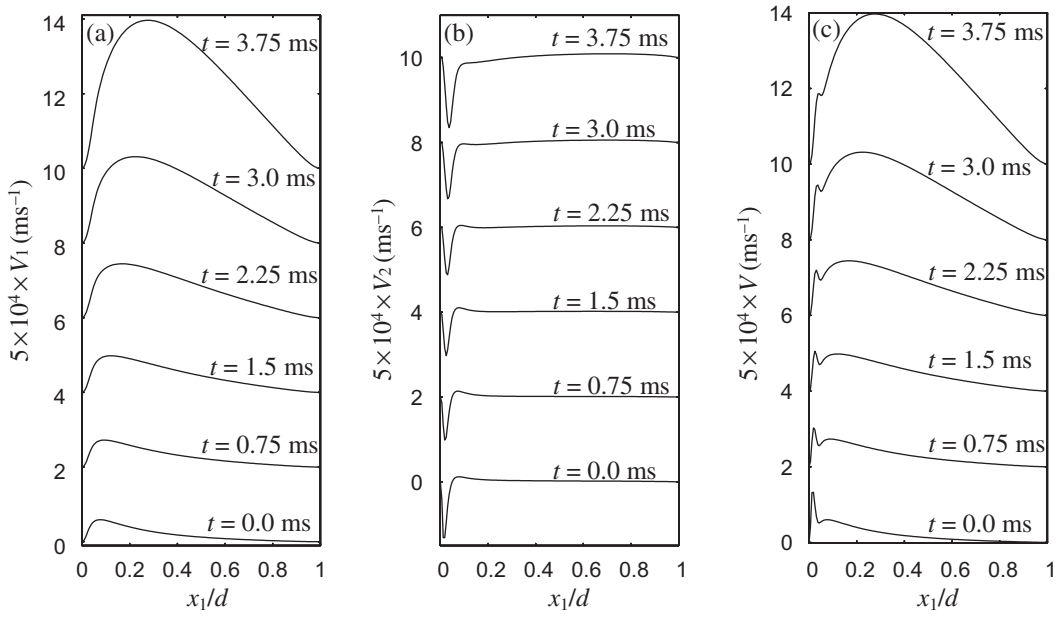

Figure 6. Profiles along the x_1 axis at $x_2/L = 0.5$ of V_1 (a), of V_2 (b) and $V = ||\mathbf{V}||$ (c) for different times; for clarity, the curves are translated by a multiple of 2. Calculated with $B = 4$ T, $\rho = 2$, $L = 250$ μm and $d = 50$ μm.

By definition (see Equation (11)) the source term is large within the misaligned region and vanishes outside this region. Remembering that no backflow is expected for a null source term, we may wonder why large backflow arises outside the misaligned region. The answer lies in the mathematical properties of partial differential equations, whose rigorous analysis is out of the scope of this work. Such equations describe some complex link between the cause (here the director configuration) and its effect (here the backflow). For example, in potential theory it is well known that the solution of a Poisson equation, $\nabla^2\Phi = \rho$, may be cast in the form $\Phi(\mathbf{r}) = \int \mathrm{G}(\mathbf{r}, \mathbf{r}')\rho(\mathbf{r}')\mathrm{d}\mathbf{r}'$ where $\mathrm{G}(\mathbf{r}, \mathbf{r}')$ is a Green function [16]. This integral relationship evidences the functional and non-local link between cause and effect: thus the source ρ placed at $\mathbf{r}'$ produces an effect (or a field) at $\mathbf{r} \neq \mathbf{r}'$ so that a field exists even in a region free of charge ($\rho = 0$). The main difference between the equation for the velocity (see Equation (9)) and a Poisson equation is the existence of the pressure term associated with the incompressibility condition; we can, nevertheless, admit that some similar functional and non-local link between the director configuration and the velocity arises as well; for that reason we should not be surprised to find a flow outside the misaligned region and this conclusion should be valid at any times.

3.4 Description of the reorientation process for $t > 0^+$ in the configuration C1

In the earlier times of the reorientation, the initial double roll extends transversally until reaching the opposite plate. This is evidenced by the time evolution of the transversal profile of V_1 shown in Figure 6. During this period, some inversion walls normal to the plates develop within the region occupied by the flow. More precisely, the first one develops at $x_2/L = 0.5$, i.e. in front of the maximum misalignment, as evidenced in Figure 7 showing the longitudinal profile of n_1 close to the plate ($x_1/d = 0.12$) and at the very beginning of the reorientation ($t = 0.75$ ms). An inversion wall in formation is evidenced by the change of

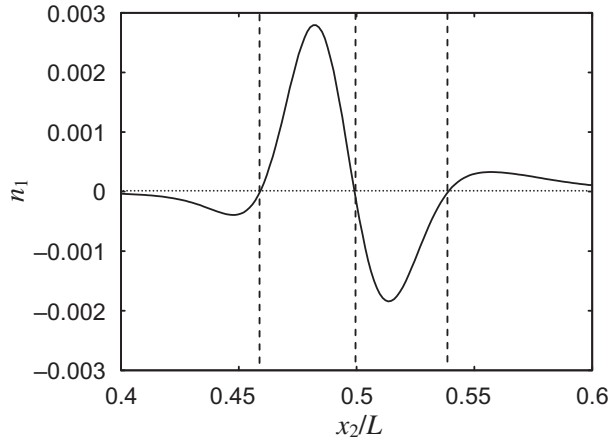

Figure 7. Profile along the x_2 axis of n_1 at time $t = 0.75$ ms for $x_1/d = 0.12$. An inversion wall is clearly being formed at $x_2/L = 0.5$. We can see the start up of two additional inversion walls where n_1 changes its sign at approximately $x_2/L \approx 0.46$ and at $x_2/L \approx 0.54$. It is worth comparing this figure with Figure 8 showing the profile $V_{1,2}$ at the same position but at time $t = 0^+$.

sign of n_1. Indeed, under the effect of the torque due to the effective aligning field (parallel to the electric field) n_1 increases (decreases) as soon as n_1 is positive (negative). Figure 7 also evidences two other less advanced inversion walls in formation at two symmetric positions with respect to the first one, namely, $x_2/L \approx 0.46$ and $x_2/L \approx 0.54$. It is instructive to compare the profile of n_1 at an earlier time of the reorientation (like that shown in Figure 7) with the longitudinal profile of $V_{1,2}$ at time $t = 0^+$ shown in Figure 8. It appears that both curves have a very similar pattern, which suggests that the term proportional to $V_{1,2}$ in Equation (1) is responsible for the nucleation of the inversion walls.

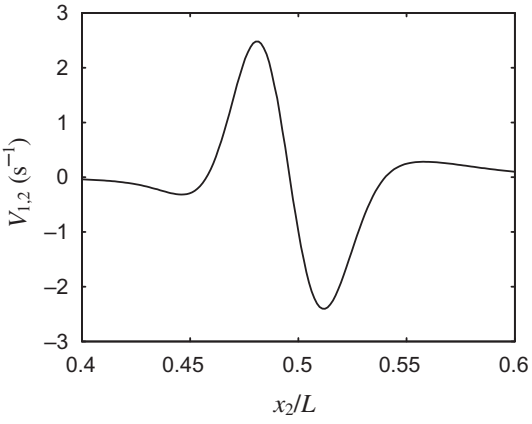

Figure 8. Profile along the x_2 axis of the velocity gradient $V_{1,2}$ at time $t = 0^+$ for $x_1/d = 0.12$.

Figures 2(b) and 3(b) show the 2D director and velocity profiles, respectively, at time $t = 7.5$ ms. In Figure 2(b) the inversion wall at $x_2/L = 0.5$ is already visible although not completely formed, while in Figure 3(b) two rolls are well-defined. Subsequently, new inversion walls develop at approximately equal intervals of distance and equal intervals of time. This behaviour is clearly shown in Figure 9 which represents the longitudinal profile of n_1 at $x_1/d = 0.5$ for different times. The time evolution of the pattern for n_1 may be described as two wave fronts propagating along the x_2 axis toward each end of the sample. After the passage of the wave-front the director has adopted a steady orientation, i.e. n_1 takes the values +1 or –1 except in a thin region where it goes rapidly from +1 to –1 (the inversion wall). In contrast, before the passage of the wave-front the director stays aligned with the magnetic field. Finally within the wave-front the director is in transit from the initial unstable orientation toward the final steady orientation. For $B = 4$T, $\rho = 2$ and $d = 50$ μm, the velocity of the wave-front is found to be about 6 mm/s.

Figure 10 shows the profile of V_1 along x_2 at the same times and x_1 abscissa as for the profiles of n_1 shown in Figure 9. It appears that the region where the flow is important coincides with the two wave-front regions in the director profiles. Accordingly, the time dependence of the V_1 profile resembles the propagation in opposite directions of two solitons whose positions coincide with the wave-front for n_1. This behaviour may be understood as follows. Far at the

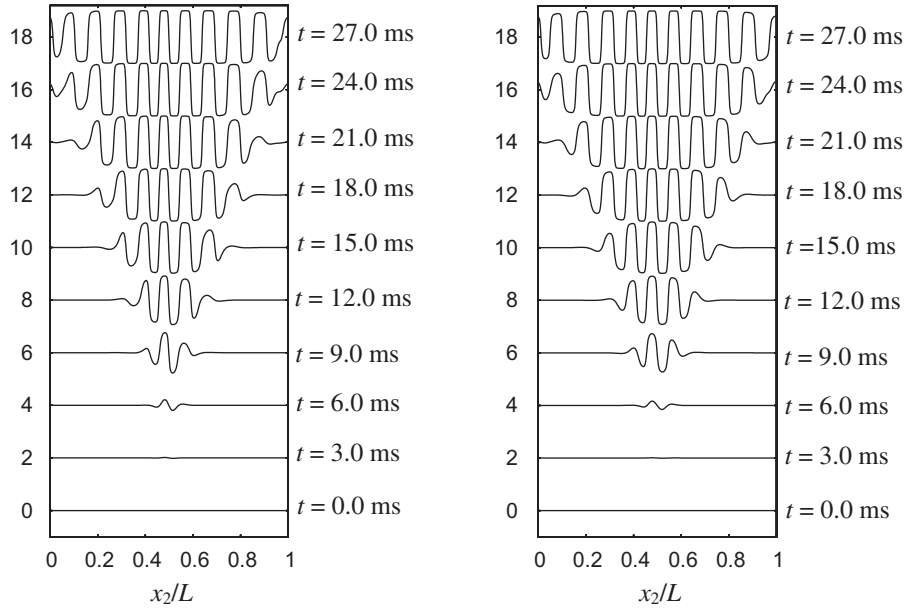

Figure 9. Profiles along the x_2 axis of n_1 at $x_1/d = 0.25$ (left) and $x_1/d = 0.5$ (right) for different times; for clarity, the curves are translated by a multiple of 2. Calculated with $B = 4$ T, $\rho = 2$, $L = 250$ μm and $d = 50$ μm. The velocity of the wave front is about 6 mm s^{-1}.

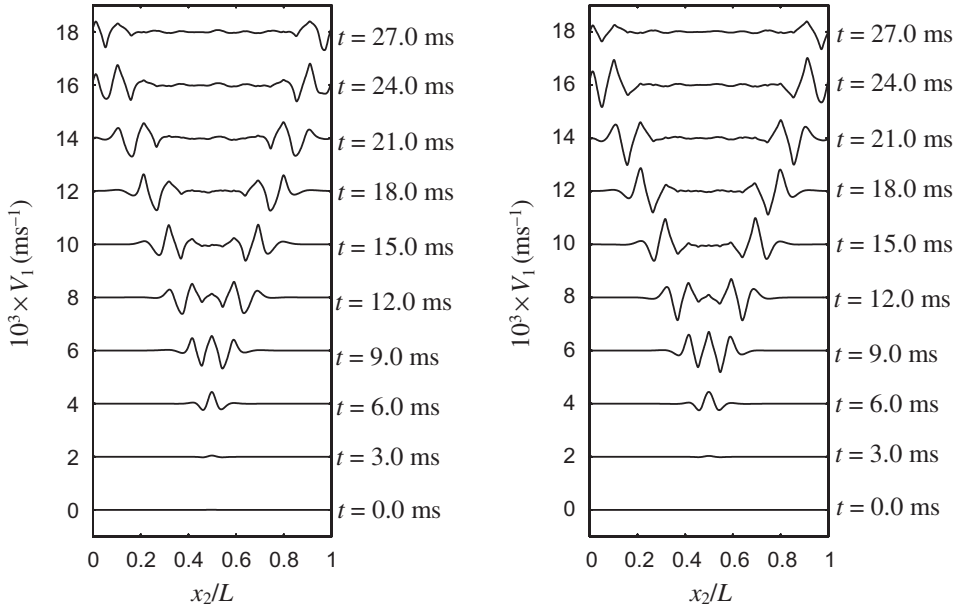

Figure 10. Profiles along the x_2 axis of V_1 at $x_1/d = 0.25$ (left) and $x_1/d = 0.5$ (right) for different times; for clarity, the curves are translated by a multiple of 2. Calculated with $B = 4$ T, $\rho = 2$, $L = 250$ μm and $d = 50$ μm.

back of the wave-front the director has reached an equilibrium state in which flow should vanish. On the other hand, far in the front of the wave-front no flow arises because we are too far from a non-steady and inhomogeneous region (i.e. a region where $\nabla \times \mathbf{S} \neq \mathbf{0}$); for the opposite reason in the region of the wave-front a flow is expected. Figures 2(c) and 3(c) show the 2D director and velocity profiles in the wave-front region at time $t = 15.75$ ms; it appears that two rolls superpose with the wave-front. In Figure 2(c) we observe the formation of an inversion wall at about $x_2/L \approx 0.69$, while in Figure 3(c) we observe two rolls around $x_2/L \approx 0.69$ as well. This feature is general; in the wave-front region the flow always exhibits at least two (or three) adjacent rolls with different magnitudes and opposite vorticities. The rolls are elongated along a direction normal to the plates while filling the space between the plates. On the other hand, the longitudinal extension and the distance between two consecutive inversion walls are comparable, namely, $\Delta x_2/L \approx 0.05$ with $L = 500$ μm, as evidenced in Figures 2(c) and 3(c).

The propagation of the roll arises as follows: in general, three adjacent rolls superpose with one wave-front with different magnitude, one being very weak in comparison with the other two; the weak roll is either a roll that has almost vanished or a roll that starts to emerge. For example, two intense rolls are clearly observed in Figure 3(c) while a less intense roll is also visible at the top of this figure. We can call R_a, R_b and R_c the three visible rolls at a given time, with R_a at the back of the wave-front and R_c at the front of the wave-front. With increase of time the roll R_a vanishes (the director stabilises in this region of the sample) while the roll R_c reinforces; when the roll R_a has completely disappeared a new roll R_d starts to emerge in front of the roll R_c, leading to the new system of three rolls R_b, R_c and R_d replacing the initial system R_a, R_b and R_c, and the same behaviour repeats periodically until the band pattern has invaded the whole sample. After a sufficiently long time a periodic director pattern without flow results, characterised by a set of (quasi) equidistant inversion walls parallel to the electric field; the walls start from one plate and end at the other plate. The periodic pattern for n_1 and n_2 at time $t = 30$ ms is shown in Figure 11. This structure seems stable but, as shown later, this stability is somewhat artificial due to some very particular anchoring condition (anchoring orientation parallel to the magnetic field when $\theta_0 = 0$ in Equation (13)).

It is of interest to determine which parameters influence the band width. We first note that all the bands do not have exactly the same width; it appears that the width of the first band developing in front of the misaligned region is strongly influenced by the longitudinal extension of this region; in contrast, the bands that appear later seem less and less influenced by the size of the misaligned region. We conclude that far from the misaligned region the band width tends towards an intrinsic width. Due to the limited size of the sample used for the numerical simulation, we have examined more precisely the dependence of the width

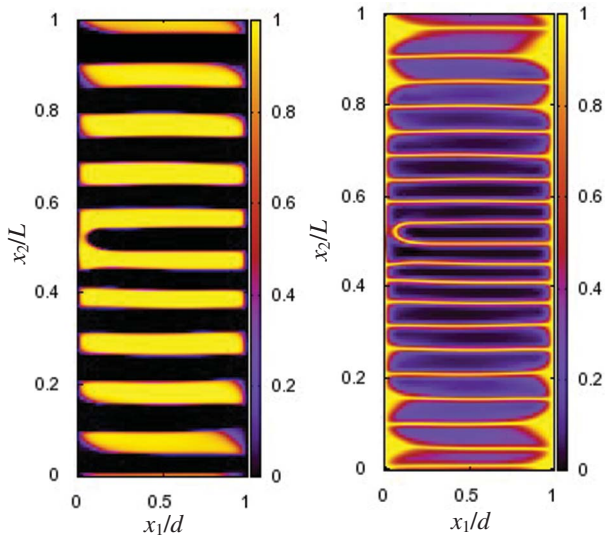

Figure 11. Profiles of n_1 (left) and n_2 (right) at time $t = 30$ ms. The inversion walls are shown by the white lines for the profile of n_2; except close to $x_2/L = 0.5$ the inversion walls are straight lines starting at one plate and ending at the opposite plate. Calculated with $B = 4$ T, $\rho = 2$, $L = 250$ μm and $d = 50$ μm.

of the third band from that appearing initially (in front of the misalignment at $x_2 = x_{20}$); we found that its width is independent of the parameter ρ that defines the strength of the electric field (or the effective field), but on the other hand a clear dependence on the distance d between the plates is evidenced. Figure 12 shows this dependence, which is roughly linear; moreover, we note that the width of one band is more or less half the distance between the plates.

3.5 *Other misalignment configuration of type C1*

It is worth considering some misalignment within a thin layer in contact with the plate at $x_1 = 0$. This situation is obtained by setting $\theta_0 \neq 0$ in Equation (13) defining the director anchoring at $x_1 = 0$. Indeed, that entrains an angle between the director on the plate and the magnetic field so that the primary initial state (at time $t = 0^-$) obtained by simple relaxation under the effect of the magnetic field alone exhibits a thin inhomogeneous layer in contact with the whole plate in which the director orientation varies from the anchoring orientation on the plate to the field orientation in the bulk. A more particular case is obtained by setting moreover $A = 0$ in Equation (13); in this latter case there is no longitudinal gradient of the director field; as a result, the velocity at time $t = 0^+$ is parallel to the plates. The fact that $V_1 = 0$ and $V_2 \neq 0$ (which seems contradictory with what we claimed in Section 3.3 for $\theta_0 = 0$ and $A \neq 0$) may be understood as follows. The homogeneity

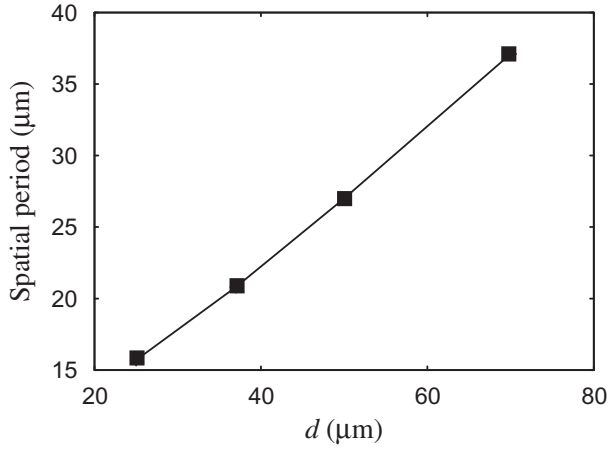

Figure 12. Spatial period as a function of the distance d between the plates. It is the depth of the third band appearing from the first one in front of the misalignment region. Calculated with $B = 4$ T, $\rho = 2$.

of the director along x_2 entrains the same homogeneity for the velocity. Hence, the incompressibility condition $V_{1,1} + V_{2,2} = 0$ entrains $V_{1,1} = 0$ or equivalently $V_1 = \text{const.}$, therefore since V_1 vanishes on the plates it vanishes everywhere. The fact that $V_2 \neq 0$ in this case is due to the infinite length of the misaligned layer, so that we can no longer assert $V_2 \to 0$ when $x_2 \to \pm\infty$ as for the case $\theta_0 = 0$ with $A \neq 0$.

The main result with $\theta_0 \neq 0$ and $A = 0$ is the absence of any band pattern; the initial misaligned layer parallel to the plates broadens uniformly, i.e. by keeping the homogeneity along x_2, until reaching the opposite plate. However, this configuration, being unstable with respect to fluctuations with gradients along x_2, cannot describe real systems. The case $\theta_0 \neq 0$ and $A \neq 0$ yields to a behaviour intermediate between the two previous ones, namely, $\theta_0 = 0$ with $A \neq 0$ and $\theta_0 \neq 0$ with $A = 0$. A periodic band pattern develops as for the case $\theta_0 = 0$ with $A \neq 0$, but in the first stage the initial misaligned layer in contact with the plate expands towards the bulk, similarly to the case $\theta_0 \neq 0$ and $A = 0$; however, this development is stopped by the appearance of the bands. As a result the inversion walls do not reach the plates at $x_1 = 0$. Since an inversion wall cannot stop within the bulk without involving a defect, two consecutive inversion walls join together in the vicinity of $x_1 = 0$, leading to an open loop starting from $x_1 = d$ and ending at another point on the plate at $x_1 = d$. Figure 13,

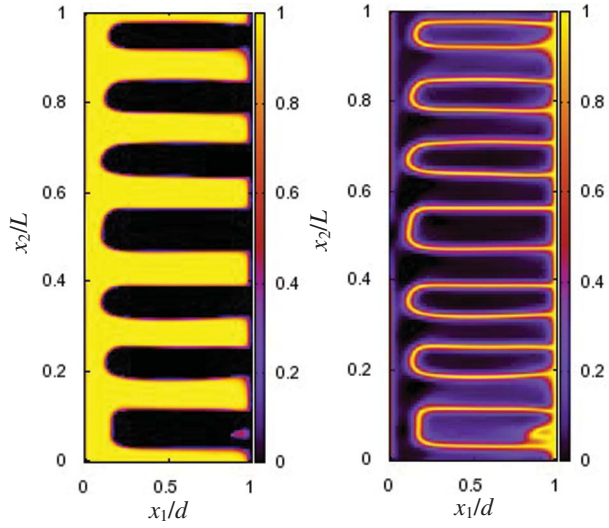

Figure 13. Profiles of n_1 (left) and n_2 (right) at time $t = 30$ ms. The inversion walls are shown by white lines in the profile of n_2; the inversion walls are open loops starting at the right plate and ending at the same plate. Note the difference with Figure 11. This structure is not completely stable, subsequently the loops shrink. Calculated with $B = 4$ T, $\rho = 2$, $L = 200$ μm and $d = 50$ μm.

showing the 2D profiles of n_1 and n_2 at time $t = 30$ ms for the case $\theta_0 = \pi/4$ with $A = 0.8$, illustrates this feature. Note the difference to Figure 11 showing the same profiles for $\theta_0 = 0$ with $A = 0.8$. Obviously, the same behaviour is expected at the opposite plate, so that the inversion walls are expected to form closed loops.

The fact that the inversion walls are no longer fixed to the plate at $x_1 = 0$ allows the system to minimise its energy by reducing the length of the inversion walls, which constitutes a second stage in the reorientation process following the formation of the bands with a notably longer characteristic time. For $B = 4$ T and $\rho = 2$, the length reduces at a rate of about 0.08 mm/s; thus for plates separated by the distance $d = 50$ μm the inversion walls disappear after a time lapse of about 300 ms (the necessary time to cover $d/2$, because in real systems the same behaviour occurs at both plates); the corresponding time for the first reorientation regime is one order of magnitude shorter for $L = 250$ μm.

3.6 *Mechanism of band formation*

With the remarks and observations made in previous sections we are able to describe the mechanism leading to the formation of the inversion walls more accurately:

(1) At time $t = 0^+$ the initial local misalignment generates a flow in a region notably more extended than the region where the misalignment arises.

(2) Accordingly, at time $t = 0^+$ there is a flowing region where the director is homogeneous and normal to the aligning field $\sqrt{\rho - 1}\,B\mathbf{e}_1$ (or equivalently parallel to the magnetic field). Within this region the elastic and field contributions to the director velocity $\partial\mathbf{n}/\partial t$ vanish so that $\partial\mathbf{n}/\partial t$ is fully determined by the gradients of the flow velocity. More precisely, according to Equation (1), out of the misalignment region we obtain

$$\begin{cases} \gamma_1 \left.\dfrac{\partial n_1}{\partial t}\right|_{t=0^+} = -\alpha_2 n_k V_{1,k} - \alpha_3 n_k V_{k,1} + \lambda n_1 \\ \gamma_1 \left.\dfrac{\partial n_2}{\partial t}\right|_{t=0^+} = -\alpha_2 n_k V_{2,k} - \alpha_3 n_k V_{k,2} + \lambda n_2. \end{cases} \tag{24}$$

By setting $n_1 = \cos\theta$ and $n_2 = \sin\theta$ the angular velocity $\partial\theta/\partial t$ is given by

$$\gamma_1 \left.\frac{\partial \theta}{\partial t}\right|_{t=0^+} = \alpha_2 \left(n_2 n_k V_{1,k} - n_1 n_k V_{2,k}\right) + \alpha_3 \left(n_2 n_k V_{k,1} - n_1 n_k V_{k,2}\right). \tag{25}$$

At time $t = 0^+$ within the part of flowing region where the misalignment is negligible we have $n_1 \approx n_3 \approx 0$ and $n_2 \approx 1$, hence the initial angular velocity may be approximated by

$$\gamma_1 \frac{\partial \theta}{\partial t}\Big|_{t=0^+} \approx \alpha_2 V_{1,2} + \alpha_3 V_{2,1}. \tag{26}$$

(3) The incompressibility condition entrains the formation of rolls in the flow at time $t = 0^+$ (see Section 3.3). For such a structure of the velocity field, the gradient $V_{1,2}$ dominates $V_{2,1}$ in some regions and, conversely, $V_{2,1}$ dominates $V_{1,2}$ in other regions; but because of the condition $|\alpha_3| << |\alpha_2|$, that is satisfied in practice for rod-like molecules, the largest angular velocity occurs within regions where $V_{1,2}$ dominates $V_{2,1}$, and it is given by $\gamma_1 \partial\theta/\partial t|_{t=0^+} \approx \alpha_2 V_{1,2}$. Thus, as revealed by the comparison of Figures 7 and 8 in Section 3.4, the gradient $V_{1,2}$ determines the start of the reorientation.

(4) When $V_1 \neq 0$, the x_2 dependence of V_1 cannot be monotonous because V_1 must vanish far from the misalignment region (i.e. when $x_2 \to \pm\infty$); accordingly, there exist at least two regions in the vicinity of the misalignment where $V_{1,2}$ is large and with opposite sign. That entrains the rotation of the director in opposite directions and an inversion wall is nucleated. Since $\alpha_2 < 0$ (see Table 1), θ increases (decreases) where $V_{1,2} < 0$ ($V_{1,2} > 0$), or equivalently n_1 decreases (increases) where $V_{1,2} < 0$ ($V_{1,2} > 0$).

(5) At time $t = 0^+$ within regions where $V_{1,2}$ dominates, the director is normal to the aligning field $\sqrt{\rho - 1}B\mathbf{e}_1$ and the corresponding torque is null; but immediately after the slight rotation of the director in the opposite direction at different positions, induced by the term $\alpha_2 V_{1,2}$ in Equation (26), the field torque amplifies the initial distortion. Subsequently, the action of the aligning field reinforces, and the formation of the inversion wall is reinforced also.

(6) When an inversion wall is in formation, a new roll develops in the region where the director is still aligned with the magnetic field and a new inversion wall is nucleated. The repetition of this process leads to the wave-front propagation. This is the so-called *progressive mode* of reorientation [2], as opposed to the *collective mode* that is induced by thermal fluctuations and develops simultaneously over the whole sample.

3.7 NMR response for different initial conditions

For an homogeneous director field with the orientation θ the deuterium NMR spectrum is composed of two lines, which we shall call the doublet, symmetric around frequency zero and with the splitting $\Delta\nu(\theta)$ defined (see Note 4) by

$$\begin{aligned}\Delta\nu(\theta) &= \Delta\nu_0 |P_2(\cos(\theta - \pi/2))| \\ &= \Delta\nu_0 |P_2(\sin\theta)|,\end{aligned} \tag{27}$$

where P_2 denotes the Legendre polynomial defined by $P_2(x) = (3x^2 - 1)/2$ and $\Delta\nu_0$ is a parameter characterising the orientational order of the nematic. The NMR spectra are built numerically from the profile $\theta(x_1, x_2)$ obtained by solving the Leslie–Ericksen equations. With each node (i, j) of the regular square grid used for the resolution of the partial differential equations is associated an elementary doublet with splitting $\Delta\nu(\theta_{ij})$, where θ_{ij} denotes the orientation of the director at the node (i, j). For the usual and simple model with Gaussian lineshapes the form of the elementary doublet associated with the orientation θ is defined by

$$I(\theta, \nu) = \sum_{\varepsilon \in \{+,-\}} \frac{1}{\sqrt{2\pi\sigma^2(\theta)}} \exp\left(-\frac{1}{2} \left(\frac{\nu - \varepsilon(\Delta\nu_0/2) P_2(\sin\theta)}{\sigma(\theta)} \right)^2 \right), \tag{28}$$

where $\sigma(\theta)$ defines the line width. In this work we used the approximate expression (see [2])

$$\sigma(\theta) = \sigma_0 + \sigma_1 \left(\sin^2\theta \cos^2\theta \right)^{2/3} \tag{29}$$

for the angular dependence of the linewidth.

In order to interpret the NMR spectra it is convenient to represent the spectrum by an analytical function of the director profile. When the director field is inhomogeneous, the NMR spectrum is a superposition of the elementary doublets $I(\theta,\nu)$ weighted by the probability density $P(\theta)$ of finding a director with orientation θ. Accordingly, the full spectrum is given by

$$I(\nu) = \int I(\theta, \nu) P(\theta) d\theta. \tag{30}$$

For the sake of simplicity, and because the spatial dependence of θ is essentially along the x_2 axis, in this work we consider the spectrum associated with an arbitrary one-dimensional profile $\theta(x_2)$. In this case, because the distribution in space of the director is uniform, the distribution $P(\theta)$ is proportional to $(d\theta/dx_2)^{-1}$. It follows that the stationary values θ_{st} of θ in the profile $\theta(x_2)$ are predominant in the distribution of θ, and consequently the corresponding doublets with the splitting $\Delta\nu(\theta_{st})$ will be predominant in the full spectrum as well. For that reason, doublets with splitting corresponding to extreme values of θ in the profile $\theta(x_2)$ are expected to emerge in the full spectrum. On the other hand, the second Legendre

polynomial appearing in the expression of the splitting $\Delta\nu(\theta)$ (see Equation (27)) also affects the pattern of the full spectrum. Indeed, a distribution of directors between θ and $\theta+\mathrm{d}\theta$ gives a distribution of splitting between $\Delta\nu(\theta)$ and $\Delta\nu(\theta) + (\partial\Delta\nu/\partial\theta)d\theta$. It follows that for the stationary values of θ in the function $P_2(\sin\theta)$ (i.e. $\theta = 0$ or $\theta = \pi/2$) the elementary doublets accumulate at the same position in the full spectrum. In other words, the doublets with splitting $\Delta\nu_0$ and $\Delta\nu_0/2$, corresponding to $\theta = \pi/2$ and $\theta = 0$, respectively, are overrepresented in the full spectrum with respect to what is expected according to the distribution of director orientation $P(\theta)$; it is why for a 2D isotropic distribution (i.e. $P(\theta) = \text{const}$) two doublets with splitting $\Delta\nu_0$ and $\Delta\nu_0/2$ emerge. The combination of these two effects (stationary orientations in the director profile and in the second Legendre polynomial) allows interpretation of the NMR spectra.

According to the above, we can distinguish two kinds of doublets in complex spectra: the *P_2 doublets* associated with the extrema of the Legendre polynomial and *θ-profile doublets* associated with the extrema of the director profile. Two P_2 doublets may exist, one with the splitting $\Delta\nu_0$ and the other one with the splitting $\Delta\nu_0/2$. Obviously, such doublets will really exist only if some director population exists with orientation parallel (splitting $\Delta\nu_0$) or normal (splitting $\Delta\nu_0/2$) to the magnetic field; it is, moreover, worth noting that the intensity of these doublets is very sensitive to the director populations in the vicinity of $\theta = 0$ and $\theta = \pi/2$, respectively. Unlike the P_2 doublets, the number and splitting of the θ-profile doublets are arbitrary because these characteristics are determined by the director profile. Thus the occurrence of one plateau around $\theta = \theta_p$ in the curve representing the profile $\theta(x_2)$ will generate a doublet with the splitting $\Delta\nu(\theta_p)$, and its intensity will be related to the spatial extension of the plateau. It follows that for an irregular profile $\theta(x_2)$ with many plateaus with different orientations, many doublets will appear; eventually, if they are sufficiently distributed they may superpose in such a way as to form a smooth and intense signal in between the inner P_2 doublet.

In this Section we investigate the NMR response associated with different initial states. In the first stage we consider an initial director field defined by one thermal fluctuation around $\theta_0 = \pi/2$ without permanent structure. Figure 14 shows the 2D profile of the director component n_1 for such a director distribution; the random character of thermal fluctuations is manifested by a granular texture. Such an initial condition leads to the classical mode of reorientation where, in brief, one Fourier mode of the thermal fluctuation defined by Equation (19) is selected and amplified

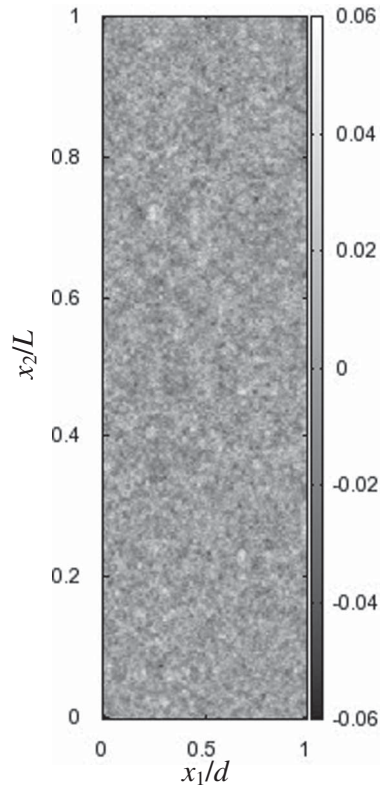

Figure 14. Two-dimensional profile of n_1 corresponding to one thermal fluctuation defined by Equation (19) with $N = 100$ and $M = 200$. Calculated with $B = 4$ T, $\rho = 2$, $L = 200$ μm and $d = 50$ μm.

[3–5]. The director and NMR responses after switching on the electric field are evidenced by the plot of the longitudinal profile of the angle θ defined by Equation (14) at $x_1/d = 0.5$ (Figures 15(a) to 15(e)) while the corresponding NMR spectra are shown in Figures 15(a') to 15(e'). For $t = 7$ ms (actually for $t \leq 7$ ms) the spectrum essentially exhibits the outer P_2 doublet with the maximum splitting $\Delta\nu_0$; thus the θ-profile shown in Figure 15(a) (where the maxima of $|\theta - \pi/2|$ are smaller than $\pi/4$) only produces some small intensity in the inside base of each peak of the doublet. For $t \geq 9$ ms (some maxima of $|\theta - \pi/2|$ slightly exceed $\pi/4$) a new doublet with a time-dependent splitting is clearly seen, although small in intensity. We may readily check that its splitting is related to the mean position of the extrema in the θ-profile according to Equation (27); indeed, for $|\theta - \pi/2| = \pi/4$ we have $\Delta\nu = \Delta\nu_0/4$. For $t = 10$ ms the splitting of the new doublet vanishes, because the maxima of $|\theta - \pi/2|$ are close to the magic angle (i.e. 54.74°) for which $P_2(\cos(\theta - \pi/2))$ vanishes, which seems to be in agreement with Figure 15(c). For $t > 10$ ms the maxima of $|\theta - \pi/2|$ exceeds the magic angle, therefore $P_2(\cos(\theta - \pi/2))$ becomes negative

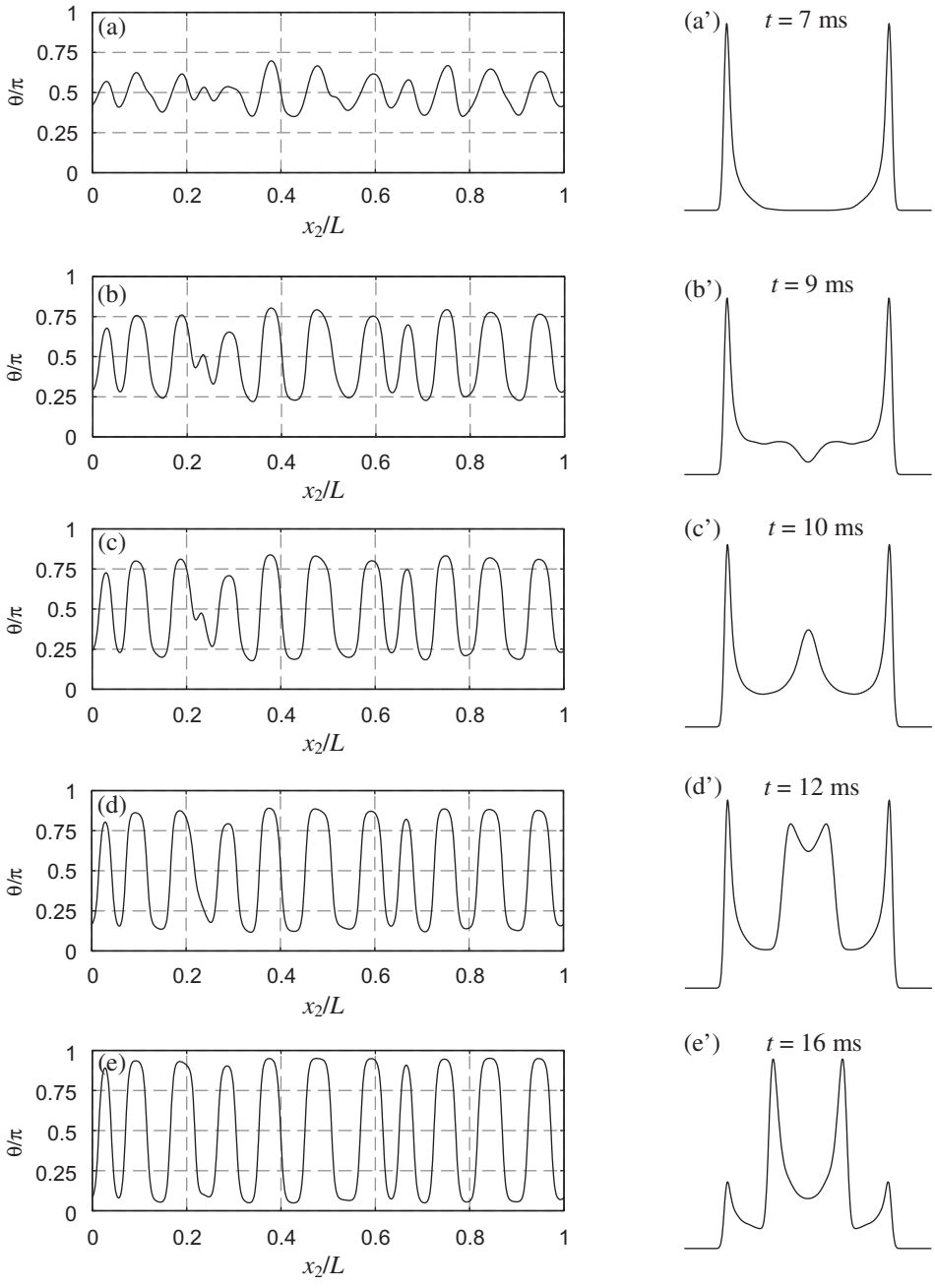

Figure 15. Longitudinal profiles of θ (defined by Equation (14)) at $x_1/d = 0.5$ for different times, namely, $t = 7$ ms in (a), $t = 9$ ms in (b), $t = 10$ ms in (c), $t = 12$ ms in (d) and $t = 16$ ms in (e). The corresponding deuterium NMR spectra at the same times are shown in (a'), (b'), (c'), (d') and (e'). At time $t = 0$ the profile corresponds to one thermal fluctuation. This figure illustrates the classical reorientation process (called the collective mode). Calculated with $B = 4$ T, $\rho = 2$, $L = 200$ μm and $d = 50$ μm.

but increases in absolute value and the splitting increases as well (see the spectra for $t = 12$ ms and $t = 16$ ms) until it reaches the value $\Delta\nu_0/2$, when the extrema of $|\theta - \pi/2|$ tends toward $\pi/2$ (see Figures 15(e) and 15(e')). Since the spectra are shown with constant maximal intensity, it is possible to observe the evolution of the relative intensities of both doublets. With increasing time, the intensity of the inner doublet increases at the expense of the outer doublet; this feature may be correlated to the formation of plateaus in the function $\theta(x_2)$ that become more and more flat with increasing time, indicating that these values of θ have a stronger weight in the distribution of θ.

Figure 16 shows the NMR response for the case accurately described in Sections 3.3 and 3.4, i.e. when a local misalignment occurs at the surface of one

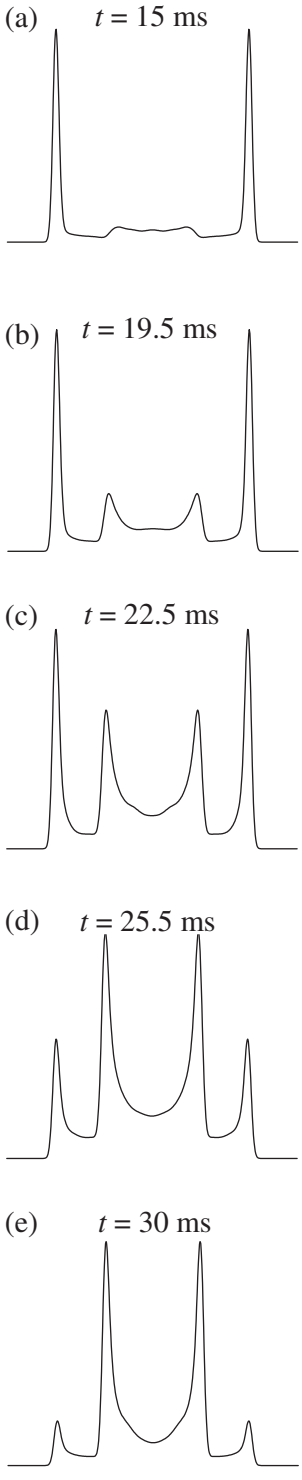

Figure 16. Deuterium NMR spectra at calculated different times, namely, $t = 15.0$ ms in (a), $t = 19.5$ ms in (b), $t = 22.5$ ms in (c), $t = 25.5$ ms in (d) and $t = 30.0$ ms in (e). At time $t = 0$ the director field exhibits one misalignment on the plate at $x_1 = 0$ as described in Section 3.3 and 3.4. This time dependence reflects the soliton regime evidenced by Figure 9; note the difference between this and Figure 15. Calculated with $B = 4$ T, $\rho = 2$, $L = 250$ μm and $d = 50$ μm.

bounding plate due to strong anchoring. The time evolution of the NMR spectrum is rather different from that shown in Figure 15 because it reflects the progressive mode of reorientation (or soliton regime) shown in Figure 9 while Figure 15 reflects the collective mode sketched in Figures 15(a) to 15(e). For the soliton regime the region fully aligned with the electric field propagates in space, which is demonstrated by the progressive increase of the intensity of the inner doublet with constant splitting equal to $\Delta\nu_0/2$. We note that the reorientation is relatively slow in comparison with the collective mode; indeed, in the soliton regime the velocity of the wave-front and the length of the sample determine the duration of the reorientation process; thus the longer the sample, (or, more precisely, the length between two consecutive misalignments), the slower the reorientation process. For the collective mode the duration of the reorientation is determined by the speed of the director rotation, which is independent of the size of the sample but depends on the selected wave-vector. It should be noted that the intermediate oscillatory region of the director profile (i.e. the wave-front) should give rise to several doublets with time-dependent splittings, as for the collective mode described previously, because of the occurrence of several extrema. However, when the length of the intermediate region is small in comparison with the spatial extension of the two other regions (the aligned and the non-aligned ones), this effect is quite negligible (actually only very small undulations can be distinguished in the spectra of Figure 16). For that reason the intensity in the central part of the spectrum is rather small, in disagreement with experimental data. When one thermal fluctuation is added in the initial state we essentially retrieve the behaviour shown in Figure 15, which indicates that the collective mode strongly dominates the progressive mode in this system. For that reason it seems difficult to account completely for the experimental data by simply assuming a local misalignment on a wall.

Figures 17(a) to 17(e) show the time evolution of the longitudinal profile $\theta(x_2)$ for $x_1/d = 0.5$ when the initial state is formed by four inversion walls not perturbed by any thermal fluctuations. The walls are located at positions x_2/L equal to 0.125, 0.375, 0.625 and 0.875, which corresponds to equidistant inversion walls when we take into account the periodic boundary conditions at $x_2/L = 0$ and $x_2/L = 1$). The corresponding NMR spectra at the same times are shown in Figures 17(a') to 17(e'). They clearly evidence the superposition of the two reorientation modes shown by Figures 15 and 16: indeed, two new doublets arise during the reorientation, one with constant splitting equal to $\Delta\nu_0/2$ and another with time-dependent splitting. The main feature of Figures 17(a) to 17(e) is the

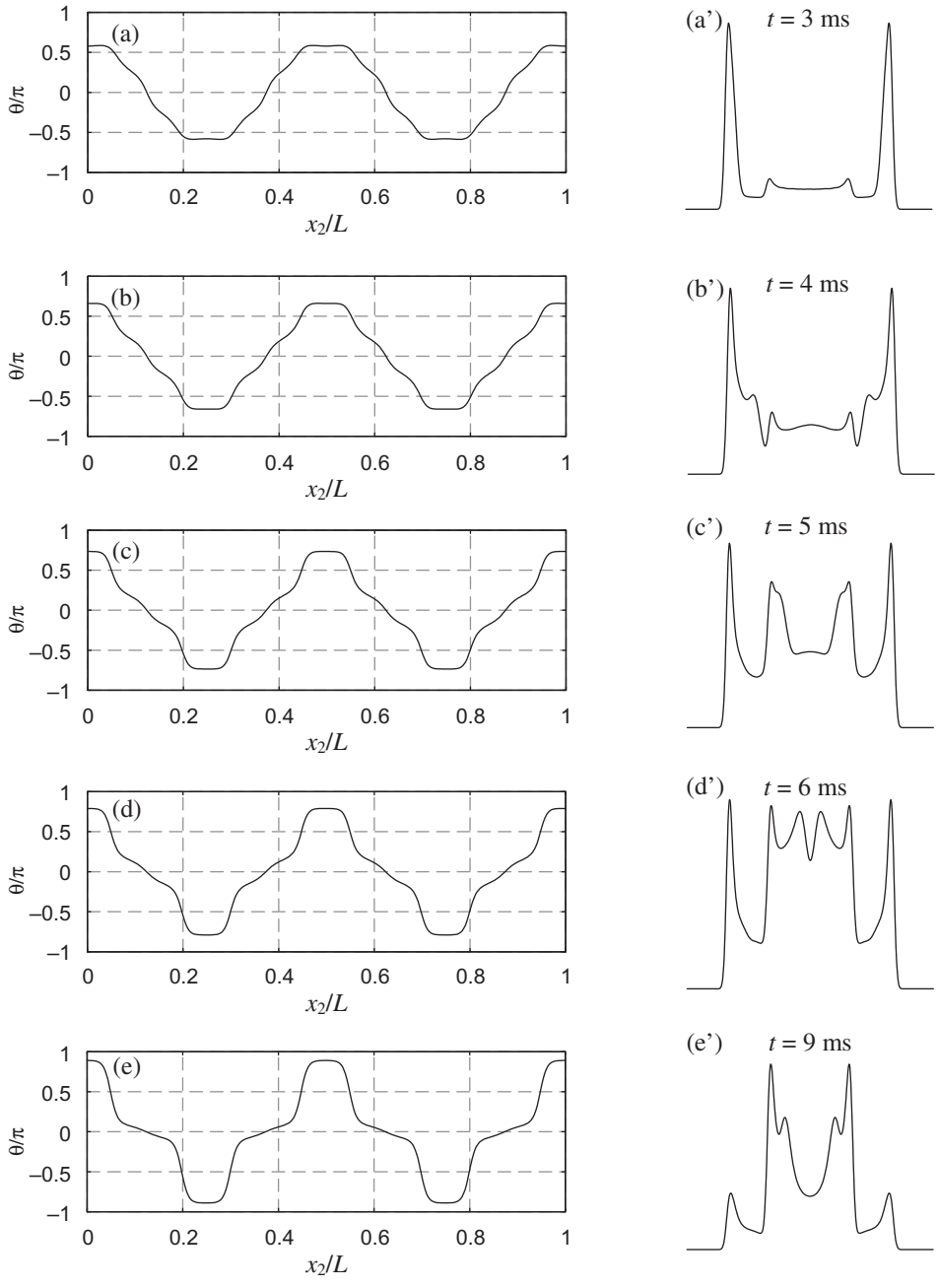

Figure 17. Longitudinal profiles of θ (defined by Equation (14)) at $x_1/d = 0.5$ for different times, namely, $t = 3$ ms in (a), $t = 4$ ms in (b), $t = 5$ ms in (c), $t = 6$ ms in (d) and $t = 9$ ms in (e). The corresponding deuterium NMR spectra at the same times are shown in (a'), (b'), (c'), (d') and (e'). At time $t = 0$ the profile $\theta(x_2)$ exhibits four inversion walls at x_2/L equal to 0.125, 0.375, 0.625 and 0.875. Calculated with $B = 4$ T, $\rho = 2$, $L = 100$ μm and $d = 50$ μm.

fact that in some regions where θ is close to $+\pi/2$ (and smaller than $\pi/2$) in the initial state (or $-\pi/2$) θ increases towards π (decreases towards $-\pi$) instead of decreasing (increasing) towards zero, which seems to be the simplest way to relax toward the new equilibrium state (i.e. $\theta = 0$ in the whole sample). This feature is similar to that evidenced by Figure 5 in Martins and Véron [2], namely, the director rotates in one direction opposite to what we would expect when considering the field and elastic forces only. This complex behaviour is indeed an effect of backflow as evidenced by comparing Figure 17 with Figure 18, obtained for the same conditions except that the backflow has been cancelled (i.e. solving Equation (1) with $\mathbf{V} = \mathbf{0}$). Indeed, without backflow the director relaxes towards the fully homogeneous state without passing by a complex metastable state with inversion walls. It should be noted that these two kinds of

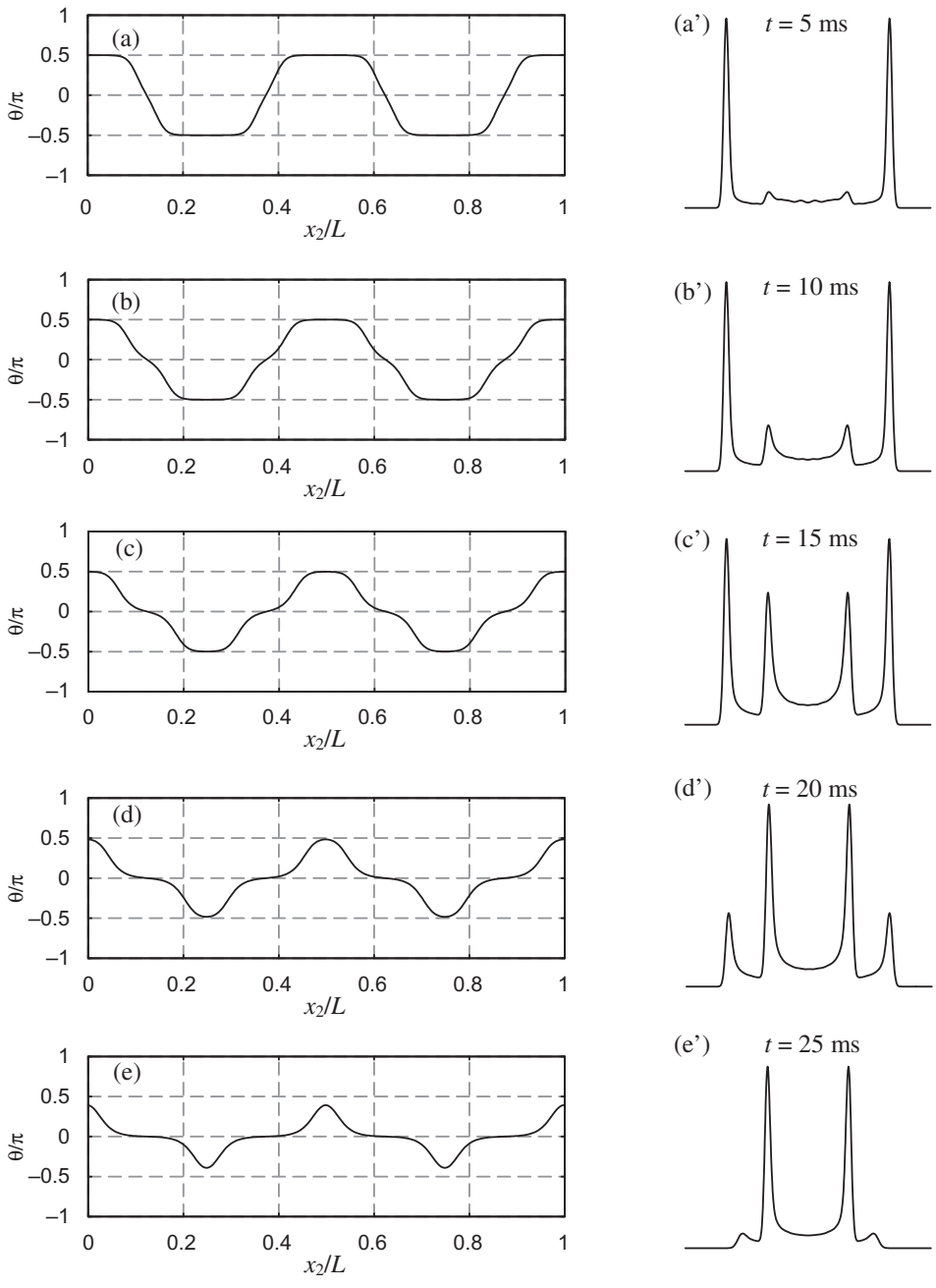

Figure 18. Longitudinal profiles of θ (defined by Equation (14)) at $x_1/d = 0.5$ for different times, namely, $t = 5$ ms in (a), $t = 10$ ms in (b), $t = 15$ ms in (c), $t = 20$ ms in (d) and $t = 25$ ms in (e). The corresponding deuterium NMR spectra at the same times are shown in (a'), (b'), (c'), (d') and (e'). At time $t = 0$ the profile $\theta(x_2)$ exhibits four inversion walls at x_2/L equal to 0.125, 0.375, 0.625 and 0.875. Calculated with $B = 4$ T, $\rho = 2$, $L = 100$ μm and $d = 50$ μm.

relaxation (i.e. the true relaxation with backflow and the false relaxation without backflow) produce different NMR responses (compare Figures 17(a') to 17(e') with Figures 18(a') to 18(e')). Without backflow the initial doublet progressively vanishes while simultaneously the doublet corresponding to a director aligned with the electric field progressively increases; this response is similar to that obtained with the soliton mode (see Figure 16), although resulting from a different mechanism. On the other hand, we note that with backflow the relaxation is notably faster (compare Figure 17(e') with Figure 18(b')). Remarking that integer values of θ/π correspond to director alignment with the electric field while half integer values correspond to director alignment with the magnetic field, it appears that the points where the

curve of the function $\theta(x_2)$ intersects the line $\theta = 0$ correspond to the core of the inversion walls. We observe that some portion of the curve $\theta(x_2)$ around $\theta = 0$, initially close to the vertical, pivots around the intersecting point until it becomes horizontal. This feature may be interpreted as an expansion of the core of the wall in a way similar to the growth of an initial cluster aligned with the electric field (cluster mode). It turns out that Figure 18 may be also interpreted as reflecting the cluster mode. It follows that without backflow the cluster mode dominates, while with backflow the cluster mode contributes to the doublet with splitting $\Delta\nu_0/2$ but it is not dominant. Note, moreover, that cluster and soliton modes have similar NMR responses (compare Figures 16 and 18) and may be considered as different manifestations of the

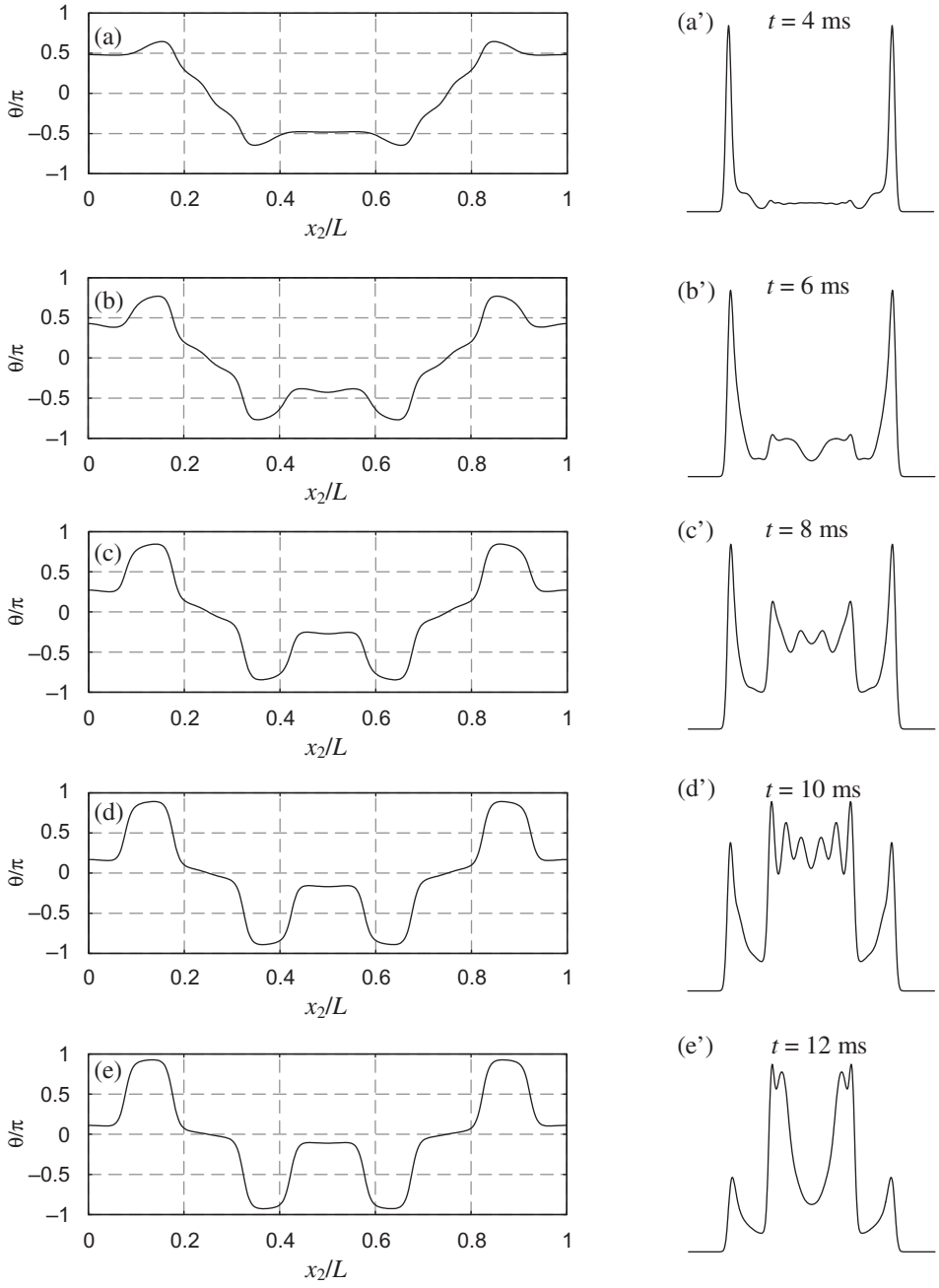

Figure 19. Longitudinal profiles of θ (defined by Equation (14)) at $x_1/d = 0.5$ for different times, namely, $t = 4$ ms in (a), $t = 6$ ms in (b), $t = 8$ ms in (c), $t = 10$ ms in (d) and $t = 12$ ms in (e). The corresponding deuterium NMR spectra at the same times are shown in (a'), (b'), (c'), (d') and (e'). At time $t = 0$ the profile $\theta(x_2)$ exhibits two inversion walls at x_2/L equal to 0.25 and 0.75. Calculated with $B = 4$ T, $\rho = 2$, $L = 100$ μm and $d = 50$ μm.

so-called *progressive mode* of reorientation. Figure 19, obtained with two inversion walls placed at x_2/L equal to 0.25 and 0.75 for the same total length L as used in the simulation that produced Figure 17, shows similar results. Nevertheless, some small discrepancies arise as, for example, the number of doublets evidenced in the spectrum at time $t = 10$ ms in Figure 19(d').

The spectrum in Figure 19(d') for $t = 10$ ms, which exhibits four inner doublets, is analysed more carefully in Figure 20. Remembering that any plateau in the θ-profile generates one doublet in the spectrum, it is possible to relate the peaks with particular portions of the θ-profile. It turns out that the profile at $t = 10$ ms is formed roughly by several plateaus (eventually slightly inclined) that can be divided into three categories, each generating one doublet. The inclined plateau marked with the letter A corresponds to part of the θ-profile that pivots around the point $\theta = 0$ (cluster mode); it gives the doublet with a constant splitting equal to $\Delta\nu_0/2$ (population in the vicinity of $\theta = 0$ a stationary point of the second Legendre polynomial). The plateau marked with the letter B corresponds to the first extremum in the wave-front of the soliton mode, while the plateau C corresponds to the second extremum with slightly smaller amplitude; this portion of the θ-profile at equal distance from the two initial walls is also a region where the two solitons coming from the two initial inversion walls meet. The position of the plateaus B and C are not exactly symmetric with respect to $\theta = \pm\pi/2$ and so they give two different doublets.

Figures 21 and 22 show the director and NMR response for two inversion walls separated by a distance of 100 μm (i.e. $L = 200$ μm in this simulation), while in Figures 17 and 18 the walls are separated by 25 μm, and in Figure 19 by 50 μm. On the other hand,

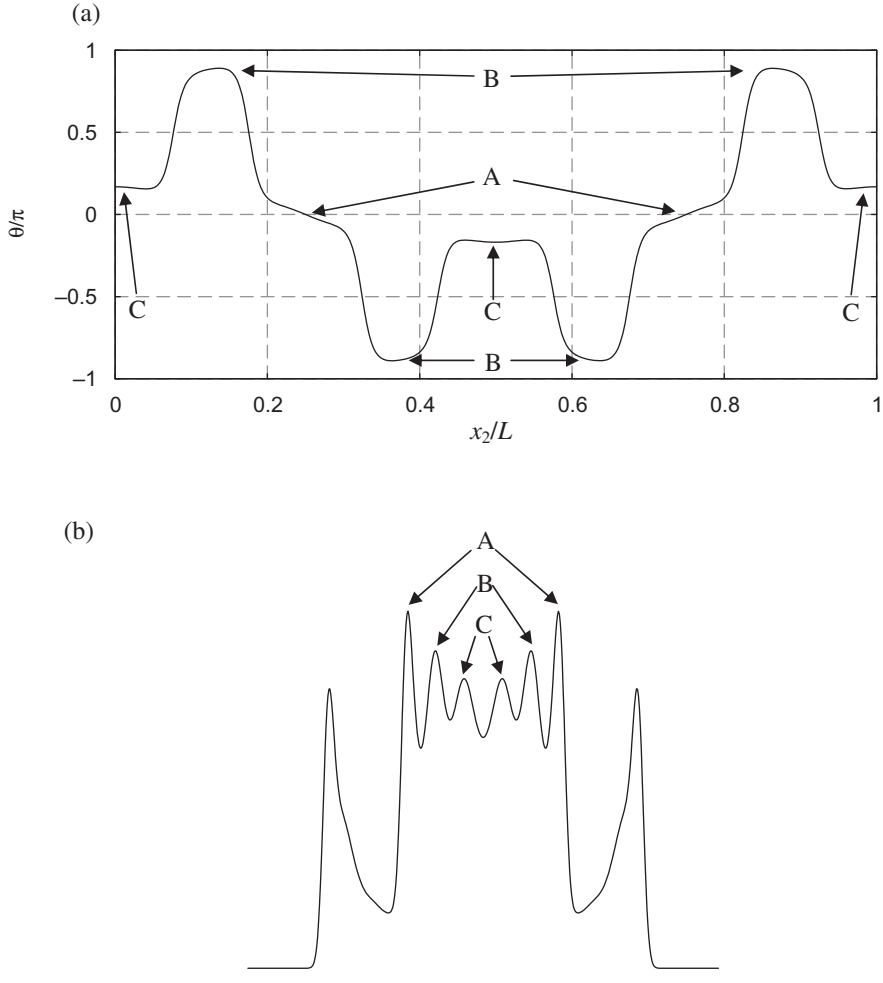

Figure 20. Longitudinal profile of θ in (a) and the corresponding deuterium NMR spectrum in (b) corresponding to that in Figure 19 for $t = 10$ ms. The three inner doublets marked with the letters A, B and C are associated with three kinds of quasi-plateaus in the θ-profile indicated by the arrows. It is worth noting that this kind of director profile yields high intensity in the central part of the spectrum.

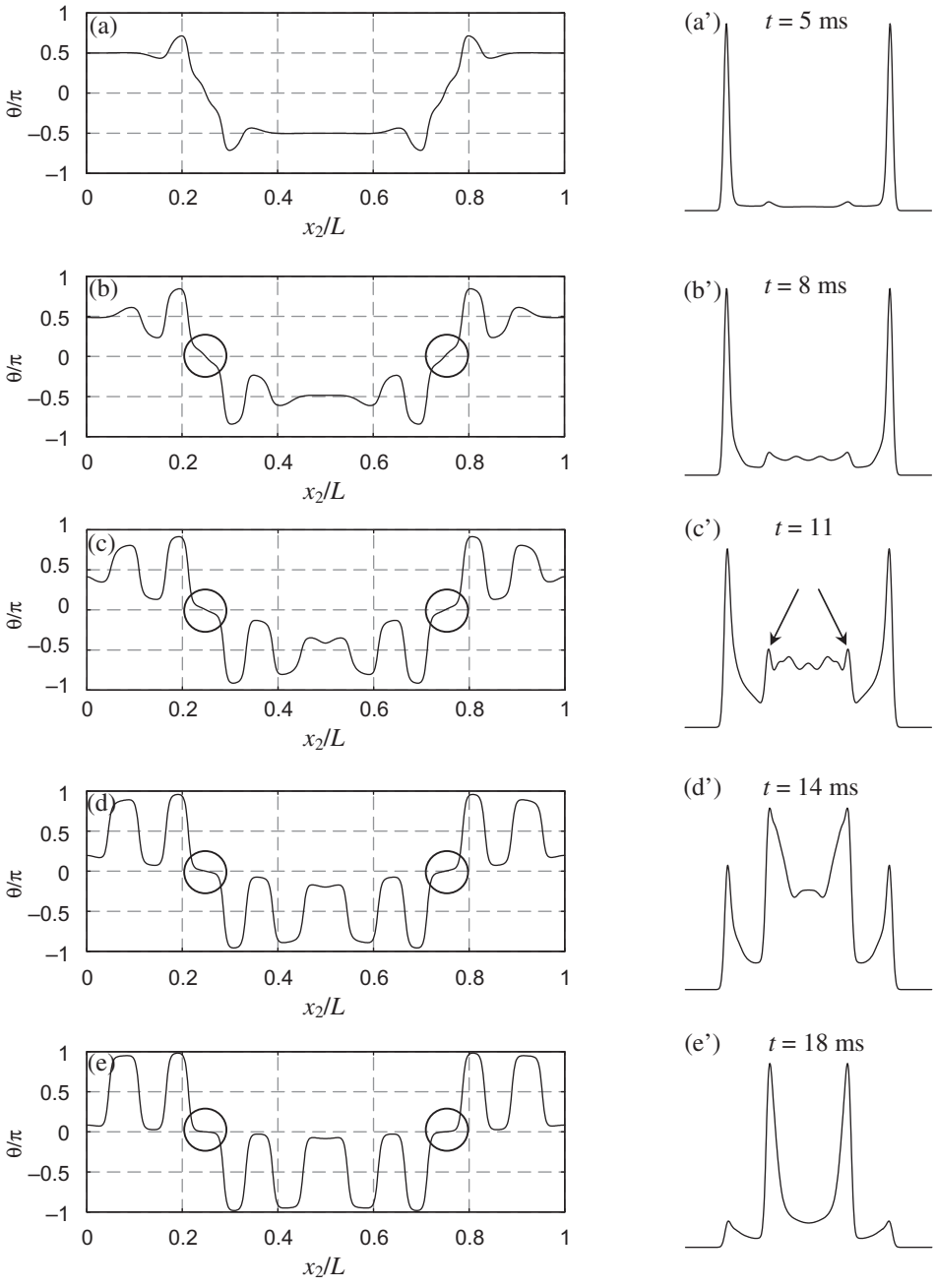

Figure 21. Longitudinal profiles of θ (defined by Equation (14)) at $x_1/d = 0.5$ for different times, namely, $t = 5$ ms in (a), $t = 8$ ms in (b), $t = 11$ ms in (c), $t = 14$ ms in (d) and $t = 18$ ms in (e). The corresponding deuterium NMR spectra at the same times are shown in (a'), (b'), (c'), (d') and (e'). At time $t = 0$ the profile $\theta(x_2)$ exhibits two inversion walls at x_2/L equal to 0.25 and 0.75. The circles indicate the portion of the θ-profile yielding the doublet with the splitting $\Delta\nu_0/2$ indicated by arrows in Figure 21c'. Calculated with $B = 4$ T, $\rho = 2$, $L = 200$ μm and $d = 50$ μm.

one thermal fluctuation is also applied to the initial state in the case shown in Figure 22. Due to the longer distance between walls, in Figures 21(a) to 21(e) the development of the soliton mode is visible between each initial inversion wall. As for Figure 18(d') a complex structure appears in the spectrum of Figure 21(c'); actually the centre of the spectrum is again more structured because a larger number of plateaus with different positions arise in Figure 21(c'). The comparison of Figure 22 with Figure 21 indicates that the effect of a thermal fluctuation is (i) to accelerate slightly the relaxation (compare Figures 21(c') and 22(c')) and (ii) to increase slightly the intensity of the central part of the spectra at the beginning of the

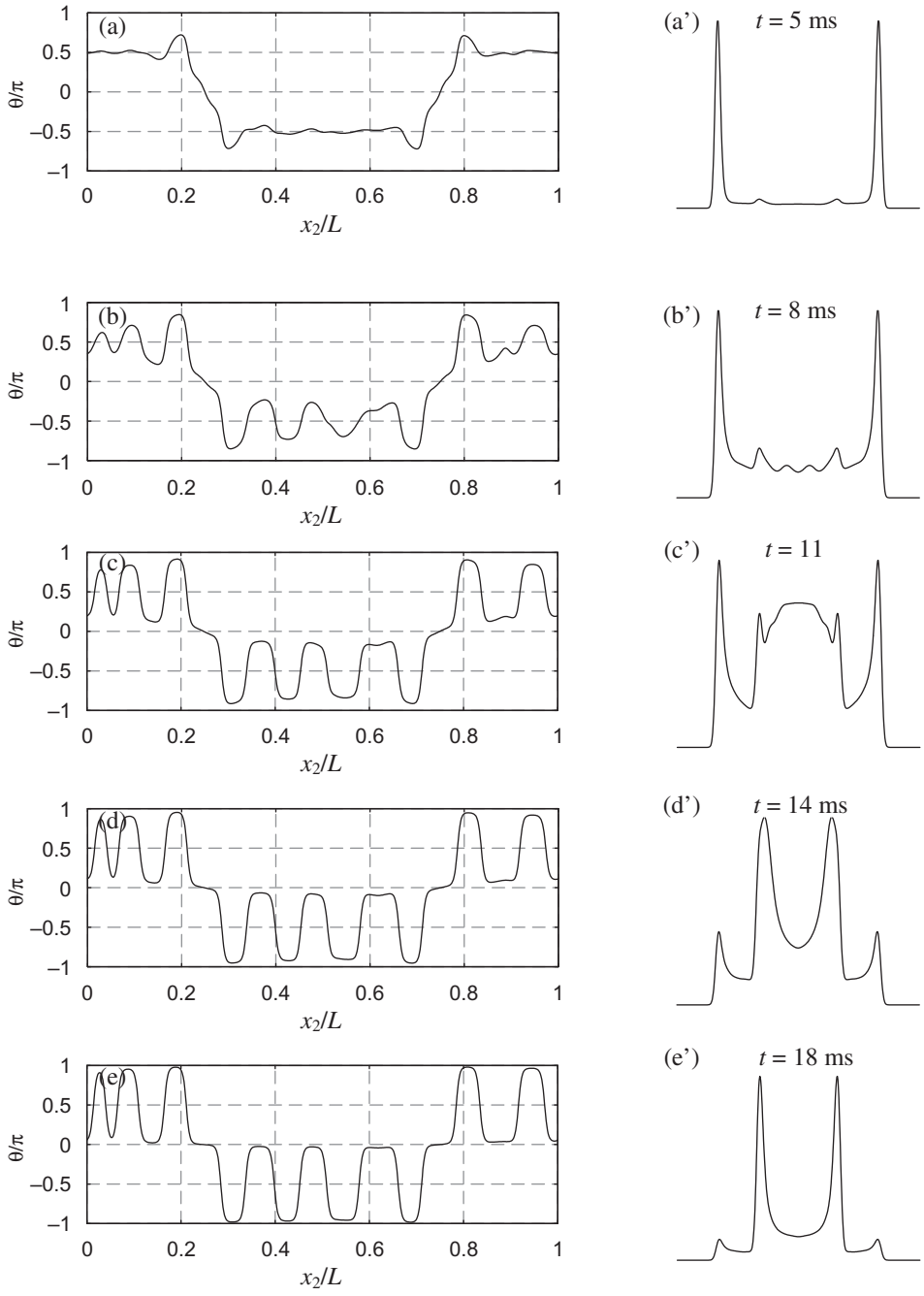

Figure 22. Longitudinal profiles of θ (defined by Equation (14)) at $x_1/d = 0.5$ for different times, namely, $t = 5$ ms in (a), $t = 8$ ms in (b), $t = 11$ ms in (c), $t = 14$ ms in (d) and $t = 18$ ms in (e). The corresponding deuterium NMR spectra at the same times are shown in (a'), (b'), (c'), (d') and (e'). At time $t = 0$ the profile $\theta(x_2)$ exhibits two inversion walls at x_2/L equal to 0.25 and 0.75 combined with one thermal fluctuation. Calculated with $B = 4$ T, $\rho = 2$, $L = 200$ μm and $d = 50$ μm.

relaxation (see the spectra at times $t = 8$ ms and $t = 11$ ms). Nevertheless, the effect of the initial thermal fluctuation is relatively weak; in other words, the soliton mode dominates the collective mode in this system; on the other hand a small contribution of the cluster mode also arises (see the circles in Figure 21), this latter mode produces the emergence of the doublet with splitting $\Delta\nu_0/2$ as soon as the reorientation starts despite the weak director population around $\theta = 0$ (n.b. effect of the second Legendre polynomial that increases the sensitivity for this orientation).

The spectra shown in Figure 16 are not satisfactory because of the lack of intensity between the inner P_2 doublet (i.e. with the splitting $\Delta\nu_0/2$) in

comparison with experimental spectra. It turns out that the spectra of Figures 17 and 19 exhibit more signal in the central region; however, they are still not satisfactory because the experimental spectra are flat in their central region while the calculated spectra show oscillations. However, accurate analysis of Figure 20 leads us to conceive this following plausible scenario. Taking into account the fact that the real system is much longer than the one simulated here, one may envisage an initial real state formed by *non-equidistant* inversion walls; in this case, different regions of the sample might reorient differently so that at particular intermediate times the positions of the plateaus might be much more distributed than in the simulations; in other words, the real director profile is expected to be less regular than the simulated one. Accordingly, this distribution of plateau position (along the x_2 axis) might generate a distribution of splitting leading to overlapping doublets so that the undulations in the central part of the spectra would vanish and a more or less intense flat signal would be observed.

4. Conclusion

This work was motivated by recent deuterium NMR data obtained with liquid crystals of low molecular mass (5CB, 8CB) confined between two parallel plates and subjected to both electric and magnetic fields as assumed in this work [6–8]. Some of these data reveal time-dependent spectra rather different from what is expected on the basis of a classical model of director reorientation assuming that the initial director misalignment is due to thermal fluctuations [3–5]. Within this classical model the reorientation occurs in the whole sample simultaneously (collective mode), which manifests in the deuterium NMR spectra by the occurrence of a doublet with time-dependent splitting. Surprisingly enough, in recent NMR results [6–8] such time-dependent splitting was not always observed; in some cases, essentially two doublets with time-dependent intensities and constant splitting were observed instead.

Since thermal fluctuations alone are not sufficient to account for the new NMR results [6–8] it appeared necessary to start with an initial state exhibiting some local misalignment stable in the presence of the sole magnetic field. Two kinds of misalignment have been considered in this work: (i) a local misalignment on a boundary plate due to inhomogeneous easy axis, and (ii) inversion walls. We have shown that a local misalignment is the source of a soliton-like mode for which the aligned region progressively invades the whole cell, a feature somewhat compatible with the observed NMR response. Moreover, an inversion wall gives rise to a cluster-like mode with small spatial extension but that nevertheless contributes notably to the development of the doublet with splitting $\Delta\nu_0/2$, again in agreement with experimental data. When one thermal fluctuation is superposed upon the initial permanent configuration, a competition between the (cluster/soliton) progressive mode and the collective mode occurs. The simulations indicate that the collective mode easily dominates the reorientation when the progressive mode is generated by an isolated punctual misalignment on a boundary plate, while it is easily dominated when the progressive mode is generated by inversion walls sufficiently close to one another. This suggests that the density of misalignment needs to be high enough to dominate the effect of thermal fluctuations, and that this situation is easier to obtain with a set of inversion walls. Finally, we believe that the occurrence of inversion walls is the key point in interpreting the new results. The problem of the origin of these inversion walls in the initial state is postponed for future work.

Acknowledgement

This work was partly supported by the European Union Science Program and "Fundação para a Ciência e a Tecnologia" (Portugal) through a post-doctoral research contract with A. Véron.

Notes

1. It results from the variation of the total free energy associated with an arbitrary parallel displacement of the director.
2. Due to the condition $n_i \partial n_i / \partial t = 0$ only the part of **h** normal to the director is effective, the part parallel to the director cancels with the term λn_i (in Equation (1)).
3. The free energy density must be integrated over the volume of the cell. Since we use a two-dimensional model, the integration along the x_3 axis reduces to a multiplication by the length of the cell along this axis assumed to be equal to L, the length along the x_2 axis (see Figure 1).
4. Note that with the notations used in this work the angle between the director and the magnetic field is $\pi/2 - \theta$.

References

[1] Véron, A.; Martins, A.F. *Thin Solid Films*, **2008**, *517*, 1380–1386.
[2] Véron, A.; Martins, A.F. *Thin Solid Films*, **2008**, *517*, 1387–1393.
[3] Martins, A.F.; Esnault, P.; Volino, F. *Phys. Rev. Lett.* **1986**, *57*, 1745–1748.
[4] Véron, A.; Gomes, A.E.; Leal, C.R.; van der Klink, J.; Martins, A.F. *Mol. Cryst. Liq. Cryst.* **1999**, *331*, 499–507.

[5] Martins, A.F.; Gomes, A.E.; Polimeno, A.; Orian, L. *Phys. Rev. E: Stat., Nonlinear, Soft Matter Phys.* **2000**, *62*, 2301–2309.
[6] Sugimura, A.; Luckhurst, G.R. In *Nanotechnology and Nano-Interface Controlled Electronic Devices*: Iwamoto, M., Kaneto, K., Mashiko, S., Eds.; Elsevier: Amsterdam, San Diego, Oxford, London, 2008; pp 313–351.
[7] Luckhurst, G.R.; Sugimura, A.; Timimi, B.A.; Zimmermann, H. *Liq. Cryst.* **2005**, *32*, 1389–1396.
[8] Luckhurst, G.R.; Miyamoto, T.; Sugimura, A.; Timimi, B.A. *Thin Solid Films* **2001**, *393*, 399–406.
[9] Leslie, F.M. *Arch. Rat. Mech. Anal.* **1968**, *28*, 265–283.
[10] de Gennes, P.G.; Prost, J. *The Physics of Liquid Crystals*, 2nd ed.; Oxford University Press: Oxford, 1993.
[11] Frank, F.C. *Discuss. Faraday Soc.* **1958**, *25*, 19–28.
[12] Parodi, O. *J. Phys.* **1970**, *31*, 581–585.
[13] Fletcher, C.A.J. *Computational Techniques for Fluid Dynamics*, 2nd ed.; Springer Series in Computational Physics; Springer-Verlag: Heidelberg, 1991.
[14] Kneppe, H.; Schneider, F.; Sharma, N.K. *Ber. Bunsenges. Phys. Chem.* **1981**, *85*, 784–789; Kneppe, H.; Schneider, F.; Sharma, N.K. *J. Chem. Phys.* **1982**, *77*, 3203–3208.
[15] Karat, P.P.; Madhusudana, N.V. *Mol. Cryst. Liq. Cryst.* **1977**, *40*, 239–245.
[16] Courant, R.; Hilbert, D. *Methods of Mathematical Physics*, Vol. II.; Wiley: New York, 1989.